


Review

# Corrosion and Corrosion Fatigue of Steels in Downhole CCS Environment—A Summary

Anja Pfennig <sup>1</sup>, Marcus Wolf <sup>2</sup> and Axel Kranzmann <sup>2,\*</sup><sup>1</sup> HTW Berlin, Wilhelminenhofstraße 75A, 12459 Berlin, Germany; anja.pfennig@htw-berlin.de<sup>2</sup> BAM Federal Institute of Materials Research and Testing, Unter den Eichen 87, 12205 Berlin, Germany; marcus.wolf@te.com

\* Correspondence: axel.kranzmann@bam.de; Tel.: +49-501-94231

**Abstract:** Static immersion tests of potential injection pipe steels 42CrMo4, X20Cr13, X46Cr13, X35CrMo4, and X5CrNiCuNb16-4 at  $T = 60\text{ °C}$  and ambient pressure, as well as  $p = 100\text{ bar}$  were performed for 700–8000 h in a  $\text{CO}_2$ -saturated synthetic aquifer environment similar to CCS sites in the Northern German Basin (NGB). Corrosion rates at 100 bar are generally lower than at ambient pressure. The main corrosion products are  $\text{FeCO}_3$  and  $\text{FeOOH}$  with surface and local corrosion phenomena directly related to the alloy composition and microstructure. The appropriate heat treatment enhances corrosion resistance. The lifetime reduction of X46Cr13, X5CrNiCuNb16-4, and duplex stainless steel X2CrNiMoN22-5-3 in a CCS environment is demonstrated in the in situ corrosion fatigue CF experiments (axial push-pull and rotation bending load,  $60\text{ °C}$ , brine: Stuttgart Aquifer and NGB, flowing  $\text{CO}_2$ : 30 L/h, +/– applied potential). Insulating the test setup is necessary to gain reliable data. S-N plots, micrographic-, phase-, fractographic-, and surface analysis prove that the life expectancy of X2CrNiMoN22-5-3 in the axial cyclic load to failure is clearly related to the surface finish, applied stress amplitude, and stress mode. The horizontal grain attack within corrosion pit cavities, multiple fatigue cracks, and preferable deterioration of austenitic phase mainly cause fatigue failure. The CF life range increases significantly when a protective potential is applied.

**Keywords:** steel; high alloyed steel; corrosion; corrosion fatigue; CCS; carbon capture and storage



**Citation:** Pfennig, A.; Wolf, M.; Kranzmann, A. Corrosion and Corrosion Fatigue of Steels in Downhole CCS Environment—A Summary. *Processes* **2021**, *9*, 594. <https://doi.org/10.3390/pr9040594>

Academic Editor: Aneta Magdziarz

Received: 3 March 2021

Accepted: 24 March 2021

Published: 29 March 2021

**Publisher's Note:** MDPI stays neutral with regard to jurisdictional claims in published maps and institutional affiliations.



**Copyright:** © 2021 by the authors. Licensee MDPI, Basel, Switzerland. This article is an open access article distributed under the terms and conditions of the Creative Commons Attribution (CC BY) license (<https://creativecommons.org/licenses/by/4.0/>).

## 1. Introduction

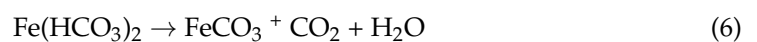
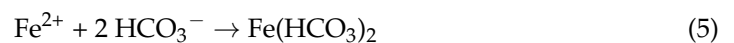
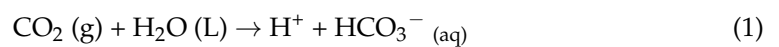
The carbon capture and storage process (CCS [1,2]) is a well acknowledged technique to mitigate climate change. Emission gases—mostly from combustion processes of power or cement production plants—are compressed into safe deep onshore or offshore geological layers. However, steels used as pipes for transport or injecting into, e.g., a saline aquifer (onshore CCS site) are susceptible to  $\text{CO}_2$ -corrosion [3–9] influenced by:

- Temperature and  $\text{CO}_2$  partial pressure;
- alloy composition and compositions of the corrosive media;
- contamination of alloy and media;
- flow conditions and injection pressure and;
- protective corrosion scales [5,6,10–21].

The corrosion resistance of various steels is mostly dependent on the composition of the alloys [22] and their heat treatment [23–25]: Ni- and Cr reduce surface corrosion phenomena [26,27] and retained austenite reduces local corrosion [26]. The higher temperature during austenitizing of martensitic steels [28–30] and annealing of lean duplex stainless steels [22,23,28] decreases the potential for local phenomena. If C-Mn (carbon) steels are heat treated to the martensitic microstructure, grain boundaries react in a  $\text{H}_2\text{S}$ -containing NaCl resulting in lower corrosion resistance compared to the ferritic or ferritic-bainitic microstructure [31].

Corrosion also leads to early failure of stainless steels that are mechanically loaded [32–34] since chemical reactions as well as local changes of lattice energy at the surface and mechanical load enhance pitting [35,36]. Pit-, selective-, and intergranular corrosion are generally correlated to the local lattice mismatch leading to crack formation [33] at dual or triple points of grain/phase boundaries with higher grain/phase boundary accelerating crack formation and propagation [32,34]. Pfennig et al. [35,36] modified a possible crack initiation first presented by Han et al. [37].

When exposing steels to the CO<sub>2</sub>-environment, the corrosion products found on the surface and within pits are similar [15,17], mostly comprising of siderite FeCO<sub>3</sub> [3,38]. The low solubility of FeCO<sub>3</sub> in water is low ( $p_{K_{sp}} = 10.54$  at 25 °C [29,37]) causing anodic iron dissolution initialized by forming of transient iron hydroxide Fe(OH)<sub>2</sub> [6,30]. The pH increases locally causing reactions (Equations (1) to (6) [15,29]) that lead to the precipitation of an internal and external ferrous carbonate film:



The literature widely describes the influence of frequency, temperature and chloride concentration [35,36,39–43], topography [44], geometric [45], and compression pre-cracking [46,47], as well as foreign impact [48–51] on the corrosion fatigue behavior and especially on the crack initiation and crack growth [45–51]. In general, corrosion processes with or without the applied mechanical stress are enhanced [49,52], especially in steels with low chromium content [6,10,11], with the presence of chloride [48,50,53,54], hydrogen [55], hydrogen sulfide (H<sub>2</sub>S) [56,57], and CO<sub>2</sub> [8,58,59]. The stress corrosion resistance under the unidirectional load in CO<sub>2</sub>-saturated brines and the endurance limit decreases with the increasing temperature, increasing mechanical load, and decreasing pH for high alloyed steels [60–62]. On the contrary, it increases with the increasing chromium content in ferritic, austenitic, and duplex steels [63], as well as the internal compressive stress in surface regions [49,64]. The martensitic microstructure shows a brittle fracture under the cyclic load [65], but improves the corrosion fatigue [66], while precipitations of copper or oxide inclusions will cause early failure already at a small number of cycles [36,67].

Standard duplex stainless steel DSS X2CrNiMoN22-5-3 (AISI 2205), usually used in operational units of desalinations plants, heat exchangers, and chemical and petroleum industries [68], is a forward-looking candidate regarding corrosion fatigue in both CCS and geothermal applications since it is highly resistant to stress corrosion cracking [69] as well as corrosive environments [70,71]. The surface quality of steels directly influences the corrosion fatigue behavior [72–80], which is improved by smooth surfaces [81], deeper plastic deformations and compressive surface stress [82–84], shot peening [85], and in ferritic stainless steel when  $R_a$  exceeded 0.5 μm [86]. The corrosion fatigue resistance of X2CrNiMoN22-5-3 under different environments [87–90] has first been tested under in situ geothermal conditions [91–93] and the results are now combined.

This paper comprises and compares summarized data of previously published work by the authors.

## 2. Materials and Methods

To examine the influence of the corrosive media on the corrosion fatigue behavior of high alloyed steels, the specimens were tested by choosing conditions similar to those

occurring during carbon capture and storage CCS (static corrosion) and conditions in geothermal energy production (corrosion fatigue).

### 2.1. Steels

Static corrosion tests at ambient pressure as well as at high pressure (100 bar) were carried out using samples of mild steel AISI 4140, 42CrMo4 1.7225 [9,15] (Table 1), martensitic and duplex stainless steels (Tables 2–6):

1. AISI 420 (X20Cr13, 1.4021) (Table 2);
2. AISI 420C (X46Cr13, 1.4043) (Table 3);
3. No AISI (X35CrMo17, 1.4122) (Table 4);
4. AISI 630 (X5CrNiCuNb 16-4, 1.4542) (Table 5);
5. AISI A182 F51 (329LN)) SAF 2205 (X2CrNiMoN 22-5-3 (UNS S31803) 1.4462) (Table 6).

In order to confirm the material's chemical composition, samples were analyzed via spark emission spectrometry SPEKTROLAB M and by the electron probe microanalyzer JXA8900-RLn (Tables 1–6).

**Table 1.** Chemical composition of 1.7225 (42CrMo4, AISI 4042), in mass percent.

Elements	C	Si	Mn	P	S	Cr	Mo	Ni	Co	Fe
acc standard <sup>a</sup>	0.38–0.45	<0.40	0.6–0.9	≤0.035	≤0.035	0.90–1.20	0.15–0.30			rest
analysed <sup>b</sup>	0.43	0.32	0.70	0.014	0.025	1.05	0.22	0.04	<0.01	97.1

<sup>a</sup> Elements as specified according to DIN EN 10088-3 in %; <sup>b</sup> spark emission spectrometry.

**Table 2.** Chemical composition of 1.4021 (X20Cr13, AISI 420A), in mass percent.

Elements	C	Si	Mn	P	S	Cr	Mo	Ni	Co	Fe
acc standard <sup>a</sup>	0.17–0.25	<1.00	≤1.00	≤0.045	≤0.03	12.0–14.0				0.20–0.45
analysed <sup>b</sup>	0.22	0.39	0.32	0.007	0.006	13.3	-	0.123	-	rest

<sup>a</sup> Elements as specified according to DIN EN 10088-3 in %; <sup>b</sup> spark emission spectrometry.

**Table 3.** Chemical composition of 1.4043 (X46Cr13, AISI 420C), in mass percent.

Elements	C	Si	Mn	P	S	Cr	Mo	Ni	Co	Fe
acc standard <sup>a</sup>	0.42–0.5	<1.00	≤1.00	≤0.045	≤0.03	12.5–14.5				0.20–0.45
analysed <sup>b</sup>	0.46	0.25	0.45	0.018	0.003	13.39	0.03	0.13	0.03	85.4

<sup>a</sup> Elements as specified according to DIN EN 10088-3 in %; <sup>b</sup> spark emission spectrometry.

**Table 4.** Chemical composition of 1.4122 (X35CrMo17), in mass percent.

Elements	C	Si	Mn	P	S	Cr	Mo	Ni	Co	Fe
acc standard <sup>a</sup>	0.33–0.45	<1.00	≤1.00	≤0.045	≤0.03	15.5–17.5	0.8–1.3	≤1.00		0.20–0.45

<sup>a</sup> Elements as specified according to DIN EN 10088-3 in %.

**Table 5.** Chemical composition of 1.4542 (X5CrNiCuNb16-4, AISI 630), in mass percent.

Elements	C	Si	Mn	P	S	Cr	Mo	Ni	Cu	Nb
acc standard <sup>a</sup>	≤0.07	≤0.70	≤1.50	≤0.04	≤0.015	15.0–17.0	≤0.60	3.00–5.00	3.00–5.00	0.20–0.45
analysed <sup>b</sup>	0.03	0.42	0.68	0.018	0.002	15.75	0.11	4.54	3.00	0.242

<sup>a</sup> Elements as specified according to DIN EN 10088-3 in %; <sup>b</sup> spark emission spectrometry.

**Table 6.** Chemical composition of 1.4462 X2CrNiMoN 22 5 3 (UNS S31803), in mass percent.

Phases	C	Si	Mn	Cr	Mo	Ni	N
$\alpha$ & $\gamma$ **	0.023	0.48	1.83	22.53	2.92	5.64	0.15
$\alpha$ *	0.02	0.55	1.59	24.31	3.62	3.81	0.07
$\gamma$ *	0.03	0.47	1.99	20.69	2.17	6.54	0.28

\* PREN  $\alpha = 37.4$ ;  $\gamma = 32.4$ ; \*\*  $p = 0.024$ ; S = 0.008.

Stainless steels 1.4043 and 1.4021 contain 13% chromium and serve as piping, shafts or axles in pumps in the geothermal energy production [38,54,94,95]. The higher carbon content of 1.4034 (0.46 mass% C) compared to 1.4020 (0.2 mass% C) most likely increases the corrosion rates.

The precipitation hardening martensitic stainless steel 1.4542 (AISI 630, X5CrNiCuNb16-4) contains 3% small grained copper [96]. Niobium and copper carbides are distributed in the layered body cubic centered (BCC) martensitic matrix [97]. The precipitation hardened microstructure shows good mechanical properties and corrosion resistance but is susceptible to stress corrosion cracking (SCC). (Note that although the strength is lower in the solution treated state, its corrosion resistance is higher [98,99]).

Stainless steel 1.4462 (X2 CrNiMoN 22-5-3 (standard duplex stainless steel, Table 6)) was continuously casted, tempered appropriately, and quenched in water resulting in a phase equilibrium of ferrite and austenite (Table 7). In general, the corrosion resistance is directly related to the percentage of austenite demonstrated by the PREN number (35.1), which is twice as high for 1.4462 than for 1.4542 [90,100].

#### Aquifer Water

To simulate the in situ geothermal condition, the geothermal aquifer water (known to be similar to the Stuttgart Aquifer [56–58,101] and Northern German Basin (NGB) [88,102]) was synthesized in a strictly orderly way to avoid the precipitation of salts and carbonates (Table 7).

**Table 7.** Chemical composition of the Northern German Basin (NGB) and Stuttgart Formation electrolyte or according to the Stuttgart Formation.

According to the Northern German Basin or according to Stuttgart Formation										
	NaCl	KCl	CaCl <sub>2</sub> × 2H <sub>2</sub> O	MgCl <sub>2</sub> × 6H <sub>2</sub> O	NH <sub>4</sub> Cl	ZnCl <sub>2</sub>	SrCl <sub>2</sub> × 6H <sub>2</sub> O	PbCl <sub>2</sub>	Na <sub>2</sub> SO <sub>4</sub>	Ph Value
g/L	98.22	5.93	207.24	4.18	0.59	0.33	4.72	0.30	0.07	5.4–6
	NaCl	KCl	CaCl <sub>2</sub> × 2H <sub>2</sub> O	MgCl <sub>2</sub> × 6H <sub>2</sub> O	Na <sub>2</sub> SO <sub>4</sub> × 10H <sub>2</sub> O	KOH	NaHCO <sub>3</sub>			
g/L	224.6	0.39	6.45	10.62	12.07	0.321	0.048			
g/L	Ca <sup>+</sup>	K <sup>2+</sup>	Mg <sup>2+</sup>	Na <sup>2+</sup>	Cl <sup>-</sup>	SO <sub>4</sub> <sup>2-</sup>	HCO <sub>3</sub> <sup>-</sup>	pH value		
	1.76	0.43	1.27	90.1	14.33	3.6	0.04	8.2–9		

#### 2.2. Static Corrosion Experiments

Coupons of the as-received and thermally treated steel qualities of 8 mm thickness, 20 mm width, and 50 mm length were exposed to: 1. CO<sub>2</sub>-saturated aquifer brine and 2. water saturated CO<sub>2</sub>.

#### Heat Treatment

One set of coupons was austenitized at 950, 1000, and 1050 °C for 30, 60, and 90 min, quenched in water and annealed at 650 °C for 30 min according to the usual heat treatment protocols. Another set of coupons was heat treated according to Table 8 [9,15–17,38,52,98,99,103–106].



**Table 8.** Heat treatment protocol for X20Cr13, X46Cr13, and X5CrNiCuNb16-4.

Heat Treatment	$T_{\text{Austenitizing}}/^{\circ}\text{C}$	$T_{\text{Austenitizing}}/^{\circ}\text{C}$	$T_{\text{Annealing}}/^{\circ}\text{C}$	$T_{\text{Annealing}}/^{\circ}\text{C}$	Time Min	Cooling Medium
	X20Cr13/X46Cr13	X5CrNi-CuNb16-4	X20Cr13 and X46Cr13	X5CrNi-CuNb16-4		
HT1 normalizing HT1	785	850			30	oil
HT2 hardening	1000	1040			30	oil
HT3 hardening + tempering 1	1040	100	550	655	30	oil
HT4 hardening + tempering 2	1040	1000	650	670	30	oil
HT5 hardening + tempering 3	1040	1000	700	755	30	oil

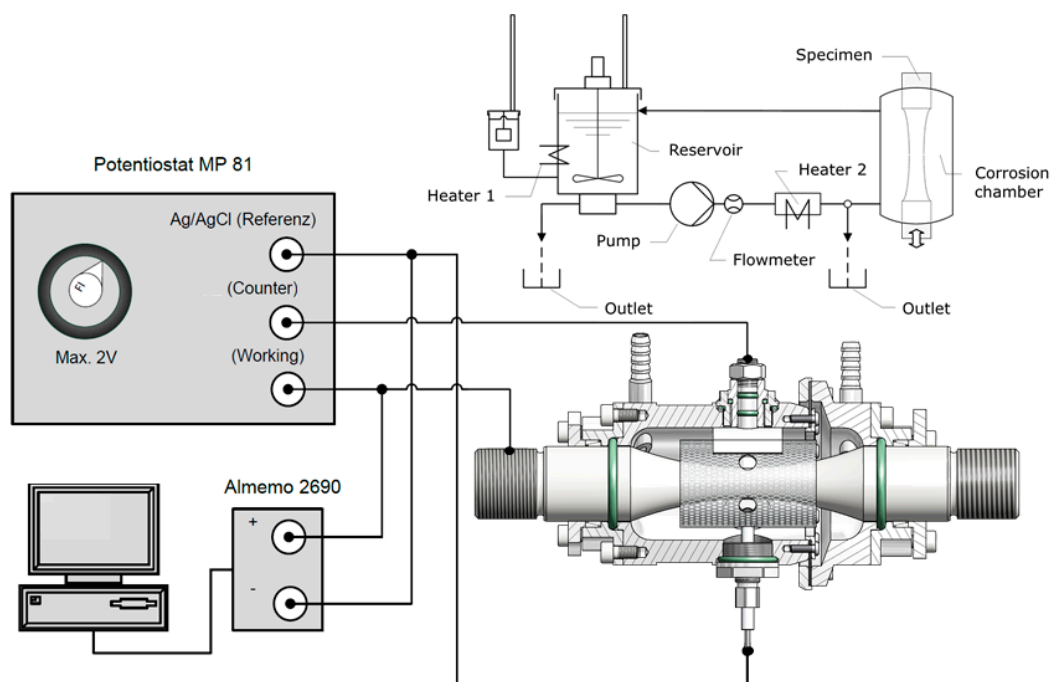
Specimens were positioned by a hole of 3.9 mm and tested in the vapor phase and liquid phase. A capillary meter GDX600\_man by QCAL Messtechnik GmbH, Munic controlled the  $\text{CO}_2$  flow (purity 99,995 vol%) into the aquifer water in ambient pressure experiments at 3 NL/h. Specimens were exposed for 700 to 8000 h using separate reaction vessels at 60 °C and 100 bar, as well as ambient pressure [9,15,16] and at 100 bar [9,15–17,38,52,98,99,103–107].

Beforehand, steel surfaces were grinded under water with SiC-paper down to 120  $\mu\text{m}$ . After corrosion testing, samples were dissected with corrosion scales (for scale analysis) and descaled with 37% HCl (for kinetic analysis). Sample parts were embedded using Epoxicure, Buehler cold resin, then cut and polished from 180 to 1200  $\mu\text{m}$  with SiC-paper under water and finished with 6 and 1  $\mu\text{m}$  using diamond paste.

### 2.3. Corrosion Fatigue Experiments

#### Test Setup

Corrosion fatigue was tested using a Schenck-Erlinger Puls PPV test machine at a frequency of 33 Hz with geothermal brine constantly flowing around the specimen. To exclude the specimen-machine interaction, the corrosion chamber is directly fixed on the test specimen [33–35,108] (Figure 1).

**Figure 1.** Schematic setup of in situ corrosion fatigue testing.

The temperature of the corrosion medium is 369 K controlled via thermal sensors in the reservoir and corrosion chamber. The specially designed electromagnetically powered gear type pumps the corrosion medium from the reservoir to the pump, into the corrosion chamber, and back into the reservoir (Figures 1 and 2) at a real flow rate of  $V^* = 2.5 \times 10^{-6} \text{ m}^3/\text{s}$  and the theoretical flow rate of  $\omega_0 = 1.7 \times 10^{-3} \text{ m/s}$  at the critical specimen section. For CCS simulation, the technical  $\text{CO}_2$  flows into the closed system at approximately 9 L/h [35,36,38,52,79,89,91,93,100,106].

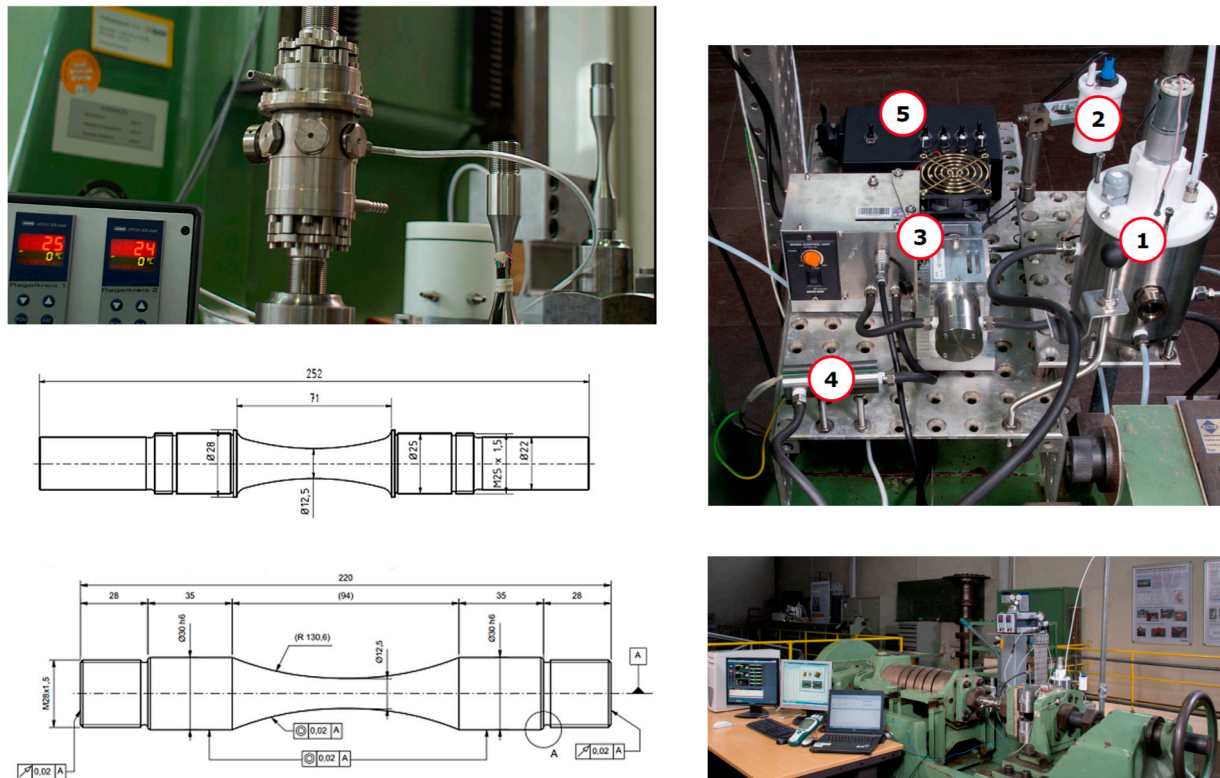


**Figure 2.** Test setup for horizontal corrosion fatigue tests (top, right). Horizontal resonant testing machine (bottom, right), periphery with gear pump, reservoir and measuring units (top, right), test specimen (bottom left), (1: Reservoir, 2: Temperature control unit, 3: Magnetically driven gear pump, 4: Heating element, 5: Control unit).

A titanium/titanium-mixed oxide electrode with no electrical contact with the specimen or chamber provides a constant potential [100,106]. An Ag/AgCl electrode fixed in a Teflon channel serves as a reference and measures the free corrosion potential [100,106].

Thirty specimens were tested in each test series between 150 and 500 MPa. Due to the rather heterogeneous fine machined surfaces (surface roughness  $R_z = 4$ ), the specimens are comparable with prefabricated parts. The fatigue strength in air (theoretically an infinite number of load cycles without failure) has a relatively smooth slope.

#### 2.4. Analysis

The morphology and layer structure of corrosion scales were analyzed using light optical and electron microscopy. The phase analysis was done via X-ray diffraction using  $\text{CoK } \alpha$ -radiation with an automatic slit adjustment, step  $0.03^\circ$ , and count of 5 s in a URD-6 (Seifert-FPM). Peak positions were identified automatically with PDF-2 (2005) powder patterns, most likely structures picked from the ICSD and refined to fit the raw-data-files using POWDERCELL 2.4 [98] and AUTOQUAN<sup>®</sup> by Seifert FPM. Three-dimensional images were produced via the double optical system Microprof TTV by the FRT characterized local corrosion. Surface corrosion rates were derived from the mass change of the coupons before and after exposure to the corrosive environment following DIN 50 905 part 1–4

(Equation (7)). Moreover, the semi-automatic analyzing program Analysis Docu ax-4 by Aquinto allowed for analyzing corrosion kinetics.

$$\text{corrosion rate} \left[ \frac{\text{mm}}{\text{year}} \right] = \frac{8760 \left[ \frac{\text{hours}}{\text{year}} \right] \cdot 10 \left[ \frac{\text{mm}}{\text{cm}} \right] \cdot \text{weight loss}[\text{g}]}{\text{area}[\text{cm}^2] \cdot \text{density} \left[ \frac{\text{g}}{\text{cm}^3} \right] \cdot \text{time}[\text{hour}]} \quad (7)$$

### 3. Results

In general, the CO<sub>2</sub> is injected in its supercritical phase [9,15,17] and reacts with salts of the aquifer to mineralize in a rather short time [88,101,102]. However, in the case of injection intermissions and technical revisions, the aquifer water may rise backwards into the borehole creating a three phase boundary consisting of CO<sub>2</sub>, aquifer water, and steel from the injection pipe. Here, the steels are most susceptible to a corrosive attack as summarized by Pfennig and Kranzmann [108]. Stable corrosion rates are reliably determined after 1 year of exposure [9,15].

#### 3.1. Surface Corrosion

Data regarding surface corrosion was compiled from references: [9,15,36,98,99,105,108].

The pitting resistance equivalent (PRE = %Cr + 3.3% Mo + 16% N) is a measure to describe the pitting resistance of high alloyed stainless steel in corrosive media containing halogen-ions (e.g., Cl<sup>-</sup>, F<sup>-</sup>, etc.). The PRE is identified by the chromium, nitrogen, and molybdenum content of a steel, the latter particularly increasing the resistance to local and crevice corrosion. A high PRE guarantees a greater reliability and broader field of application since the steel is more resistant against a corrosive attack. Both the ferrite and austenite phase of duplex stainless steel X2 CrNiMoN 22-5-3 with a high PRE number (53.1) do not deteriorate or show corrosion phenomena, neither after exposure up to 1 year to CO<sub>2</sub>-saturated Stuttgart Aquifer water [101] nor to the Northern German Basin [88,102]. The microstructural change and crack propagation under the dynamic load was analyzed in detail by Wolf et al. [52,100,109].

The influence of chromium as a corrosion resistant element is clearly shown for 42CrMo4. The stainless steel 42CrMo4 has a relatively high Mo-content of 0.22 wt% exceeding that of X46Cr13 by a factor of 7 (0.03 wt%). However, corrosion rates are high due to the low chromium content (1.05 wt%) compared to the much lower corrosion rates resulting in a smaller corrosion layer of X46Cr13 (PRE = 12.5–14.5, Cr = 13.39 wt%).

Under pressure at 100 bar corrosion rates are lower than at ambient pressure, as shown for the mild steel 42CrMo4 in Figure 3 [9,15,105,108] and martensitic stainless steels X20Cr13, X46Cr13, X35CrMo17, and X5CrNiCuNb 16-4 in Figure 4 [9,15,105,108]. Higher corrosion rates at ambient pressure may be attributed to the corrosion layer with an open capillary system (not present at 100 bar) enabling a fast mutual diffusion of ionic species as a requirement for scale growth [105].

*Corrosion scale:* The complicated multi-layered corrosion scale analyzed after exposure at ambient pressure [15,105,108] reveals a carbonate/oxide structure that mainly comprises of siderite FeCO<sub>3</sub>, goethite α-FeOOH, mackinawite FeS, and akaganeite Fe<sub>8</sub>O<sub>8</sub>(OH)<sub>8</sub>Cl<sub>1.34</sub>. Additionally, various chemically different spinel-phases and carbides (Fe<sub>3</sub>C or Cr-rich iron carbides, first described by Hünert et al. [110]) are present. Note that the corrosion products in pits are the same as in the surface corrosion layers [16,105,108].

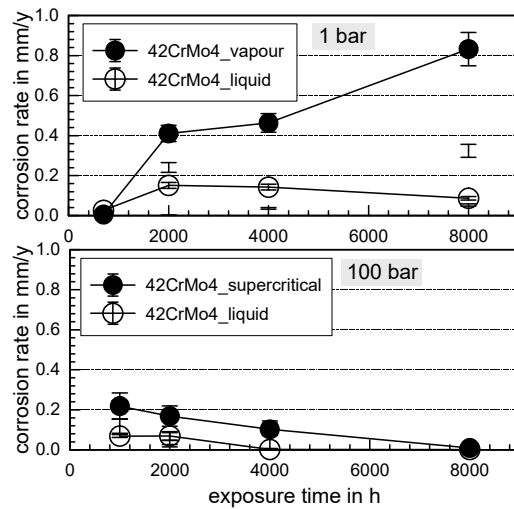


**Figure 3.** Comparison of corrosion rates of 42CrMo4 and X46Cr13 after 8000 h of exposure to aquifer brine water at 60 °C and ambient pressure, as well as at 100 bar.

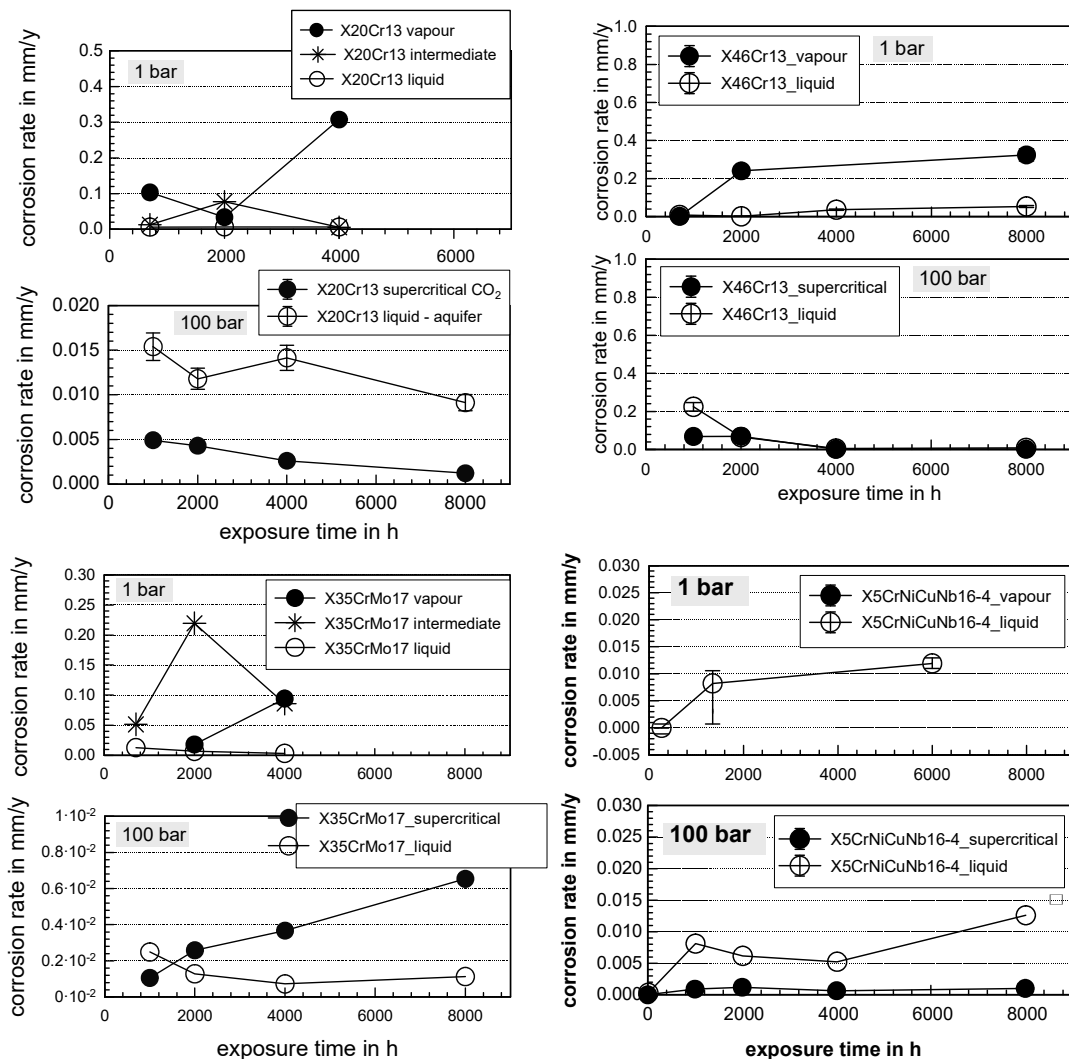


**Figure 4.** Comparison of corrosion rates in the liquid and vapor/supercritical phase after 8000 h of exposure to aquifer brine water at 60 °C and ambient pressure, as well as at 100 bar. (Up left): X20Cr13, (up right): X46Cr13 ambient pressure 100 bar, (down left): X35CrMo17-1, (down right): X5CrNiCuNb16-4.

*Exposure time:* For 42CrMo4, X20Cr13, and X46Cr13, the corrosion rates increase with time at ambient pressure and decrease with time at 100 bar. In the vapor phase at ambient pressure, the corrosion rate for 42CrMo4 doubles from 4000 h (0.45 mm/year) of exposure to 8000 h (0.8 mm/year). In the liquid phase, the exposure time has little impact on the corrosion rate. The same applies for both atmospheres at 100 bar [105,108]. This corresponds with the thickness of the precipitation layer that is greater in the vapor/supercritical than in the liquid phase. Possibly, the experimental low pressure system is not completely gas tight and excess oxygen accelerates the corrosive degradation of the steel rates as a function of time. At 100 bar, however, fast forming hydroxides [3,12,37,105,108] passivate the steel surface initially then react to form a siderite-layer that increases with time and acts as a diffusion barrier. For X5CrNiCuNb16-4 and X35CrMo17, corrosion rates generally increase slightly (at ambient pressure as well as at 100 bar) [105] attributed to the passivating layer breaking down. Although the alloy composition accounts for a stable passivating layer, additional local corrosion phenomena increase the overall corrosion rates.

*Pressure:* The corrosion rates at ambient pressure are much higher for 42CrMo4, X20Cr13, and X35CrMo4 than at 100 bar. Stainless steels X20Cr13 and X5CrNiCuNb16-4 show less dependence on pressure.

*Atmosphere with regards to pressure:* At ambient pressure, corrosion rates in the vapor phase (water-saturated CO<sub>2</sub>) are higher by a factor of 3–8 compared to the liquid phase (CO<sub>2</sub>-saturated water). At 100 bar, corrosion rates in the liquid phase can be both higher or lower than in the vapor/supercritical phase.

The atmosphere (liquid, vapor or supercritical atmosphere) does not significantly influence the general corrosive behavior. That is: It cannot be stated that the vapor/supercritical atmosphere (water saturated CO<sub>2</sub>) leads to higher or lower corrosion rates than the liquid atmosphere (CO<sub>2</sub>-saturated water). In the vapor phase, the supercritical CO<sub>2</sub> is saturated with H<sub>2</sub>O in contrast to the liquid phase where liquid H<sub>2</sub>O saturated with CO<sub>2</sub>. Although it is known that the corrosion rate increases with the increasing CO<sub>2</sub>-partial pressure [3,105,108], the explanation that higher corrosion rates in the vapor (supercritical) phase correspond with the high CO<sub>2</sub> partial pressure compared to the liquid phase with a lower CO<sub>2</sub> partial pressure does not count here.

Higher corrosion rates in the liquid phase at ambient pressure for X5CrNiCuNb16-4, X20Cr13, and X35CrMo4 and less significant for X20Cr13 and 42CrMo4 may generally be explained by slower diffusion kinetics. Moreover, when comparing phase precipitations in the supercritical phase and in water at high pressure, the diffusional flow is much slower in the water phase than in the supercritical phase. This has been explained in detail by Pfennig et al. [105,108]: Slower diffusion leads to the stable growths of the {10-10}-planes leading to the typical tabular crystal habit [105,108]. Due to the low density of the supercritical phase compared to the liquid greater diffusion rates in the supercritical phase, this enhances the nucleation of siderite crystals and results in small crystals forming a dense layer on the metal surface (Figure 5). The faster kinetics are supported by the higher CO<sub>2</sub>-partial pressure in the supercritical phase, also enhancing nucleation and therefore smaller siderite crystals [105,108].

FeCO<sub>3</sub>-grains decrease in size with the increasing pressure. However, with similar corrosion rates measured in the liquid phase and in the vapor/supercritical phase (<0.1 mm/year in the liquid and 0.03 mm/year in the vapor phase) it may be assumed that the grain size is not decisive, but the thickness of the corrosion scale counts for diffusional pathways. The corrosion rates decrease with the longer diffusion pathways. After 8000 h of exposure, the scale has grown to a diffusion barrier preventing the mutual diffusion of elements from the base material and from the CO<sub>2</sub> aquifer mixture (O<sub>2</sub> and CO<sub>2</sub> diffuse into the steel's surface and Fe<sup>2+</sup> diffuses from the metal bulk to the surface). The dissolution of the iron base material leads to an increase in the local pH at the steel surface due to the accumulation of ferrous ions that then reacts to ferrous carbonate after super-saturation at the steels surface [12]. The reaction kinetics are not significantly related to the precipitation morphologies and pressure [12,105,108], but to the oxygen partial pressure [111].



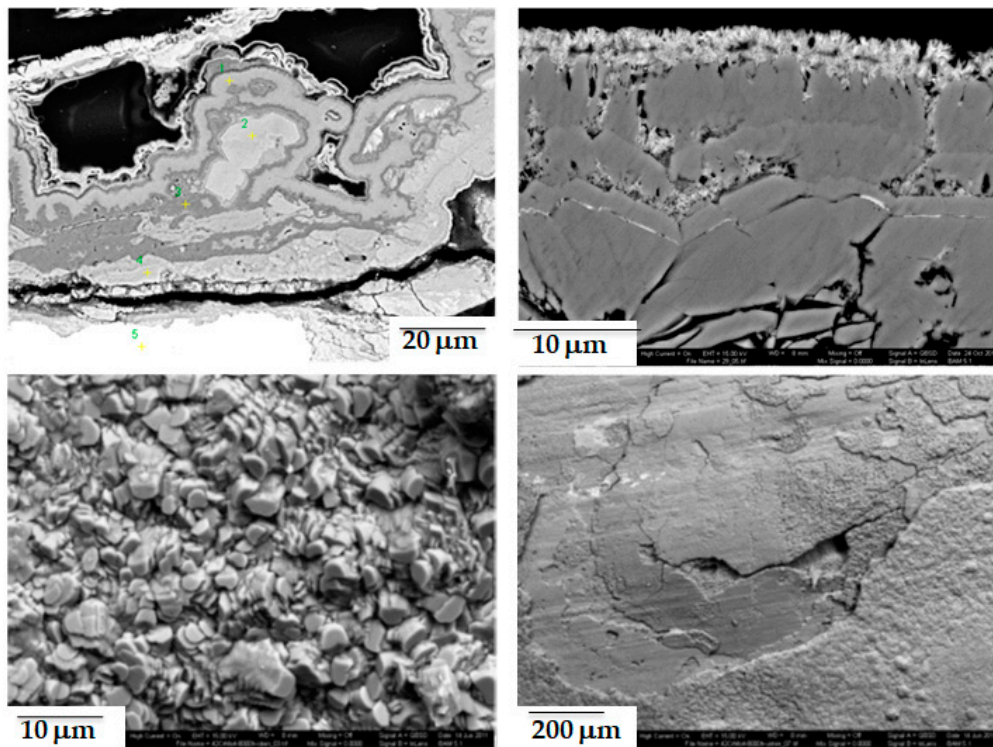


**Figure 5.** Surface precipitation on 42CrMo4 after exposure to CO<sub>2</sub> saturated saline aquifer water for 8000 h at ambient pressure and 100 bar. (Top left and right): Cross section (vapor), (bottom left): Vapor, (right): Liquid.

### 3.2. Local Corrosion

Data regarding local corrosion was compiled from references: [9,15,16,36,98,99,105,108].

Stainless steel 42CrMo4 is highly susceptible towards surface corrosion so that no pits were distinctively measured. Initial pits grow very quickly to a discontinuous surface layer that can be divided into an inner (dissolution of base metal) and outer (oxide growth on metal surface) corrosion layer covering the entire surface of the sample (Figures 5 and 6).

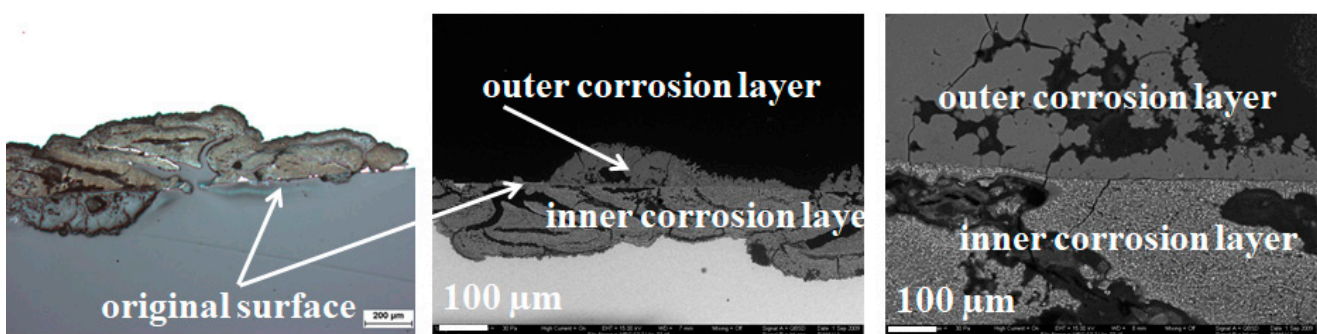
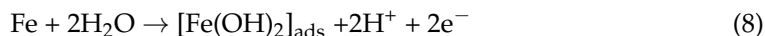


**Figure 6.** SEM micrographs of X46Cr13 after 17,200 h of exposure at 60 °C and 100 bar to water saturated supercritical CO<sub>2</sub> clearly showing the inner and outer corrosion layer.

The internal and external corrosion layer grow depending on the various carbon and oxygen partial pressures [17,36,99]. Due to mismatches of thermal expansion coefficients and large differences in surface morphologies, the corrosion layer detaches in lateral direction once a critical thickness of the surface corrosion layer is exceeded.



This local surface degradation is enhanced since oxygen vacancies, as a result of Equations (1)–(6), consolidate and condense at the hydroxide/brine interface. The dependence on the anionic concentration of the consecutive reactions has been discussed by Wei et al. [112]. As a consequence, the siderite detaches from a transient hydroxide film described in detail by various authors [6,17,26,36] with vacancies generated by carbonate ions being the main cause for the precipitation of oxygen vacancies (Equations (8) and (9)a,b):



The flowing corrosive media removes the remaining film causing the pit to grow wider and eventually covers the entire surface.

In contrast, the other steel qualities investigated showed distinct local corrosion phenomena (Figure 7) [9,15,16,36,98,99,105,108] with generally higher number of pits under aquifer water conditions. Moreover, a higher chromium content of the steels leads to a higher number of pits per  $\text{m}^2$ . (Note that these steels only show very little surface corrosion but therefore are highly susceptible to local corrosion). The number of pits formed at 100 bar, either, in  $\text{CO}_2$ -saturated aquifer water (liquid phase) or in water saturated  $\text{CO}_2$  (supercritical/vapor phase) exceeds those formed at ambient pressure by a factor of 10. This is due to the fact that after similar exposure times, the corrosion scale is much thicker when precipitated at ambient pressure and therefore complicates the analysis. Moreover, kinetics at 100 bar are faster, pressing  $\text{CO}_2$  and water onto the metal's surface resulting in a lower pH and faster local degradation of the steel [104].

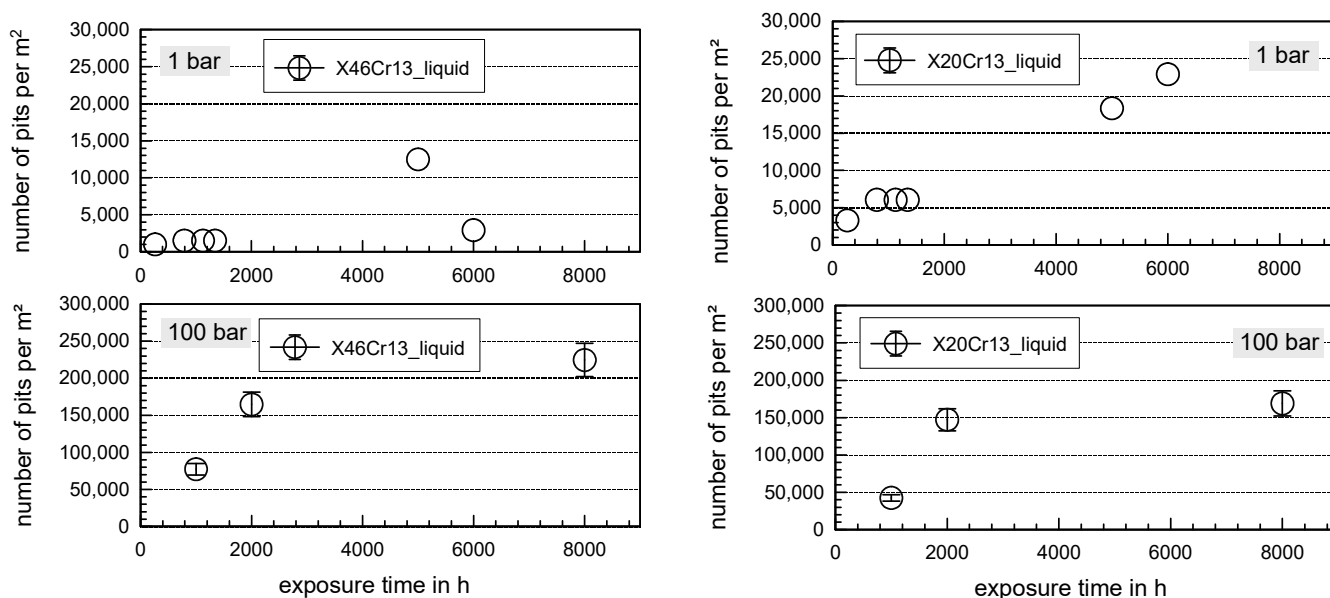
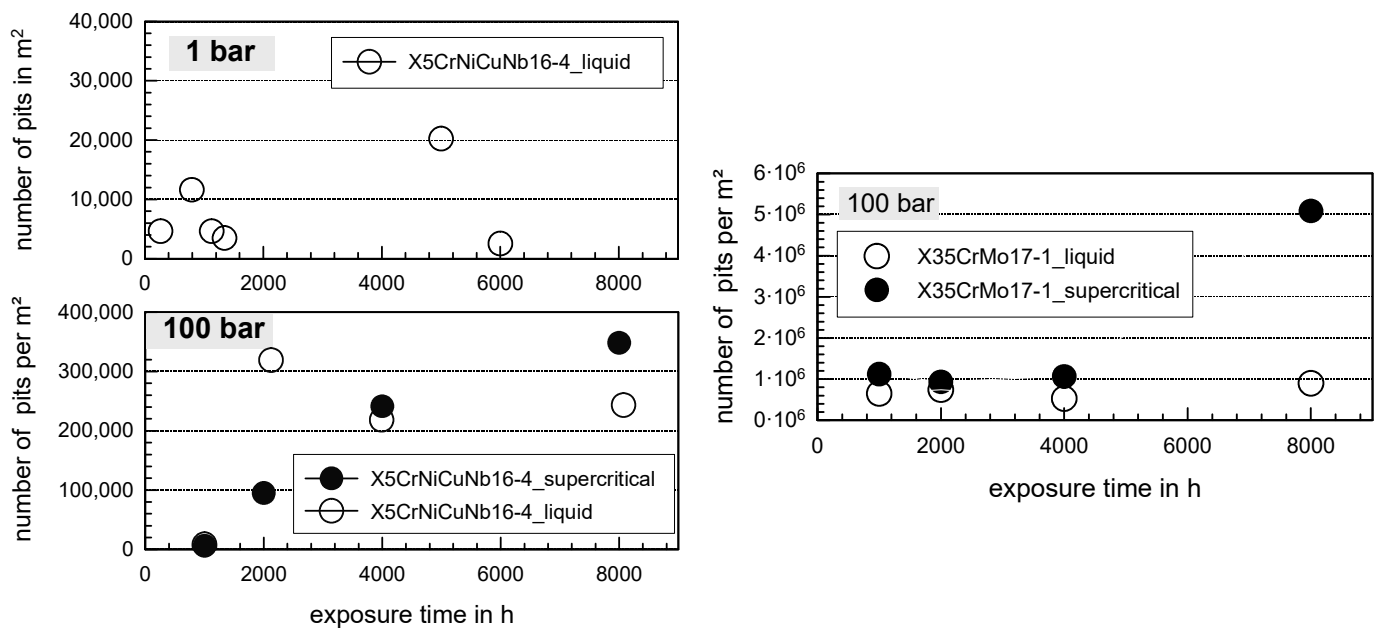


Figure 7. Cont.



**Figure 7.** Number of pits of X20Cr13 in the liquid phase after 6000/8000 h of exposure to aquifer brine water at 60 °C and ambient pressure, as well as at 100 bar. (Up left): X20Cr13, (up right): X46Cr13, (down left): X35CrMo17-1, (down right): X5CrNiCuNb16-4.

### 3.3. Influence of Heat Treatment

Data regarding the influence of heat treatment was compiled from references: [17,38,98,99,103,104,108,113,114].

#### 3.3.1. Surface Corrosion

All steels meet the requirements for pressure vessels (DIN 6601 < 0.1 mm/year), since the corrosion rate generally does not exceed 0.04 mm/year for differently heat treated X20Cr13, X46Cr13, and X5CrNiCuNb16-4—independent of the heat treatment, atmosphere (liquid, supercritical/vapor) or pressure (1 and 100 bar). At 100 bar and high CO<sub>2</sub> partial, the lower corrosion rates pressure could be a consequence of closed capillary systems within the corrosion scale. The dense layer prevents fast diffusion processes after the long exposure and sufficient thickness of the corrosion layer.

The influence of the corrosion behavior of steels on their heat treatment is well known [11,17,22,28,29,98,104]. The lowest corrosion rates and therefore good corrosion resistance regarding surface corrosion in water saturated supercritical CO<sub>2</sub> and CO<sub>2</sub>—saturated saline water are accomplished by hardening and tempering the steel at low temperature (600–670 °C) to obtain a martensitic microstructure.

Generally, surface corrosion rates increase as a function of exposure time. At ambient pressure, surface corrosion rates of heat treated X20Cr13 and X46Cr13 increase significantly (factor 3). At 100 bar, the corrosion rates do not increase when exposed for 4000 to 8000 h assuming a sufficient thick carbonate layer reduces the diffusion of ionic species into the base materials (CO<sub>3</sub><sup>2-</sup>- and O<sub>2</sub><sup>-</sup>-species) and towards the outer surface (Fe-ions) and prevents further degradation [17,104].

Except for steel coupons hardened and tempered at 700 °C, corrosion rates at 100 bar were compared to those obtained for X5CrNiCuNb16-4 (below 0.005 mm/year). Generally, corrosion rates do not differ significantly after a long exposure to the CCS environment. However, hardening and tempering at a high temperature of 700/755 °C may lead to the precipitation of Cr-carbides in X20Cr13 and X46Cr13 after a long exposure depleting the metal matrix of free chromium because passivation of the surface then hinders the base material degrades.

Generally, low corrosion rates in the liquid and even lower in the supercritical phase for X5CrNiCuNb16-4 are attributed to passivation and possibly insufficient electrolytes [38,89]. Moreover, the cathodic reactions (Equations (1) and (2)) result in a higher  $\text{H}_2\text{CO}_3$  concentration and therefore more acidic and reactive environment as in the  $\text{CO}_2$  saturated liquid phase [7,26]. Corrosion rates increase at 100 bar in the supercritical phase and remain at the same level kept in the liquid phase (0.003 mm/y after 4000 h). Depassivation after 1000 h of exposure in the supercritical phase is the result of fast reaction kinetics and carbide precipitation. The accompanied chromium depletion of the matrix (Figure 8) prohibits new passivation and degrades the material [98,113].



**Figure 8.** Left: SEM micrographs and element distribution of the ellipsoidal corrosion layer formed on X5CrNiCuNb16-4 hardened and tempered at 670 °C prior to exposure after 8000 h of exposure at 60 °C and 100 bar to water saturated supercritical  $\text{CO}_2$ .

The influence of the heat treatment is more significant at 100 bar than at ambient pressure. However, since the data is not distinct, the heat treatment for X5CrNiCuNb16-4 seems not decisive—rather the chromium content and atmosphere. Good surface corrosion resistance at ambient pressure can be attributed for steels hardened or hardened and tempered. Good surface corrosion resistance at 100 bar under supercritical  $\text{CO}_2$  conditions hardened and tempered at 670 °C (<0.001 mm/year, martensitic microstructure) and in the liquid phase normalized (ca. 0.004 mm/year, ferritic-perlitic microstructure) [98,113].

The time of austenitizing plays a significant role regarding the surface corrosion of X46Cr13 and X20Cr13 (Figure 9) but is neglectable regarding local corrosion [58,103,104,114]. Surface corrosion decreases as a function of increasing the austenitizing time and decreasing the austenitizing temperature [114]. The lowest corrosion rates were found for specimens heated to 950 °C and annealed for 30 min compared to the highest corrosion rates austenitized at 1050 °C for 60 min after 700 h [114]. The significance of the influence decreases with the increasing exposure time to a geothermal environment. After 4000 h of exposure, austenitizing becomes insignificant (Figure 9) [103,104,114].

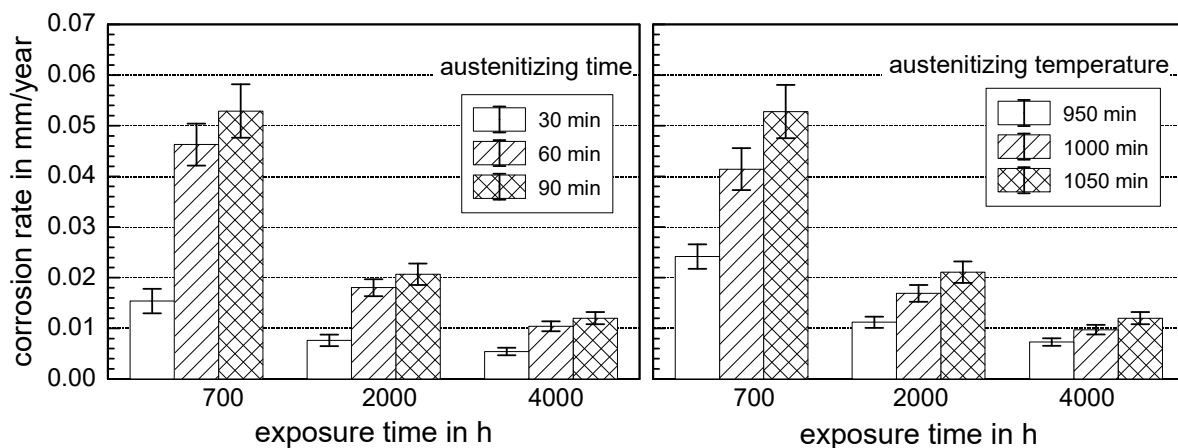


**Figure 9.** Influence of austenitizing: Surface corrosion rate (combined: X20Cr13 and X46Cr13 annealed at 650 °C for 30 min) as a function of austenitizing time and temperature prior to exposure to CO<sub>2</sub>-saturated saline aquifer water.

### 3.3.2. Pit Corrosion

Pit formation is most likely also described by Han et al. as the initial formation of Fe(OH)<sub>2</sub> (Equations (1)–(6)) [6,37] locally increasing the pH near the hydroxide film followed by the internal and external formation of a ferrous carbonate film [37]. Chlorides enhance local corrosion [46]. Additionally, dislocations, grain boundaries, and precipitation phase boundaries, such as carbides result in a local lattice mismatch thus the local boundary energy increases [36]. Therefore, the distinct microstructure itself is susceptible to a corrosive attack. When the hydroxide film is then locally damaged, e.g., at grain boundaries, pitting is initialized by dissolving the film, depassivating the base material, and finally detaching the carbonate film (Figure 10) [17,38,98,99,103,104,108,113,114].

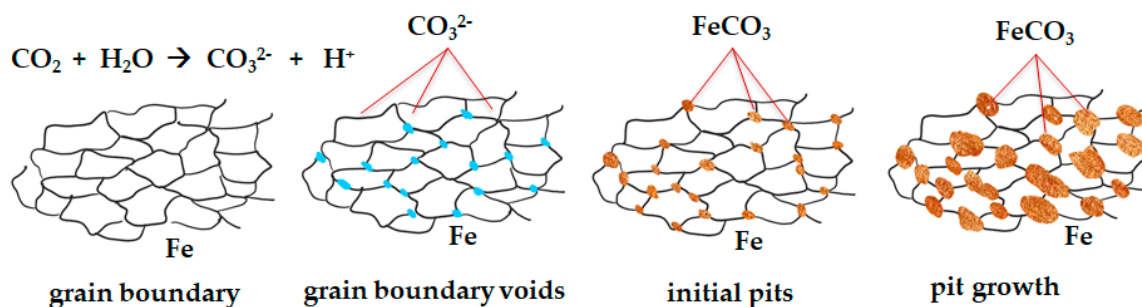


**Figure 10.** Schematic drawing of pit precipitation on injection steels initiated at grain boundaries.

Local corrosion as a function of the austenitizing time and temperature promises a better pit corrosion resistance for X20Cr13 than for X46Cr13 (X20Cr13: ca. 3508814 pits per m<sup>2</sup>, X46Cr13: ca. 9622 pits per m<sup>2</sup>). The same result applies for pit diameters revealing an average pit diameter for X46Cr13 of 249 µm, which is five times larger than the average pit on the X20Cr13 (49 µm) [54,103]. The majority of pits after 700 h of exposure are 51 to 100 µm in diameter, but the number of pits for X46Cr13 is three times higher than for X20Cr13.

Even if the maximum pit diameter of pits that precipitated on X46Cr13 succeed those precipitated on X20Cr13 by a factor of 3.5 for steel coupons austenitized at 950 °C for 90 min, the average pit diameter of both steel qualities does not differ significantly. Furthermore, there is no significant influence on the austenitizing routines prior to exposure to the CCS environment. The average pit diameter does not succeed at 100 µm after 700 h of exposure. (Note that the critical parameter to assess the influence of pit precipitation is preferably not the diameter, but the depth of pits). However, after 700 to 4000 h, the depth of pits was shown to be quite comparable and these will be evaluated more closely in the future.

At ambient pressure and at 100 bar, as well as the number of pits per unit area are not significantly influenced by the particular heat treatment (no significant lowest number of pits) [16,17,103,108,114]. Hardening and tempering between 600 and 670 °C realize the lowest number of pits after 6000 h of exposure. (Note that the pits may consolidate to a shallow pit corrosion phenomena and therefore lead to unusual low numbers of pits).

Generally, pitting is independent of the heat treatment. Steels with martensitic microstructure and higher carbon-content were developed in fewer pits with smaller maximum intrusion depths. At ambient pressure, the number of pits levels off for X20Cr13, X46Cr13, and X5CrNiCuNb16-4 (<40,000 per m<sup>2</sup>). At 100 bar, the number of pits is independent of the heat treatment and atmosphere (water saturated supercritical CO<sub>2</sub> and CO<sub>2</sub> saturated aquifer) except for coupons hardened and tempered at 670 °C. Although known as corrosion resistant, X5CrNiCuNb16-4 shows a high number of pits per m<sup>2</sup> in both atmospheres at ambient pressure and 100 bar [98].

The maximum pit depth is not influenced significantly by the heat treatment. For the heat treated specimen (Table 8), pit intrusion depths for all steel qualities were obtained metallographically and via the optical volume measurement (Figure 11). The pit depth increases with the exposure time (max. 300 µm for X20Cr13, hardened after 6000 h of exposure at ambient pressure) [38,104,105]. The average pit depths for X5CrNiCuNb16-4 is 10–250 µm after exposure at 100 bar and 60 °C (Figure 11). Normalizing and hardening + tempering at 600 °C seems to be favorable for X20Cr13 and X46Cr13 (intrusion depth: 8–25 µm), whereas hardening + tempering between 670 and 755 °C is recommended for X5CrNiCuNb16-4 (intrusion depth: 10 µm) [104].

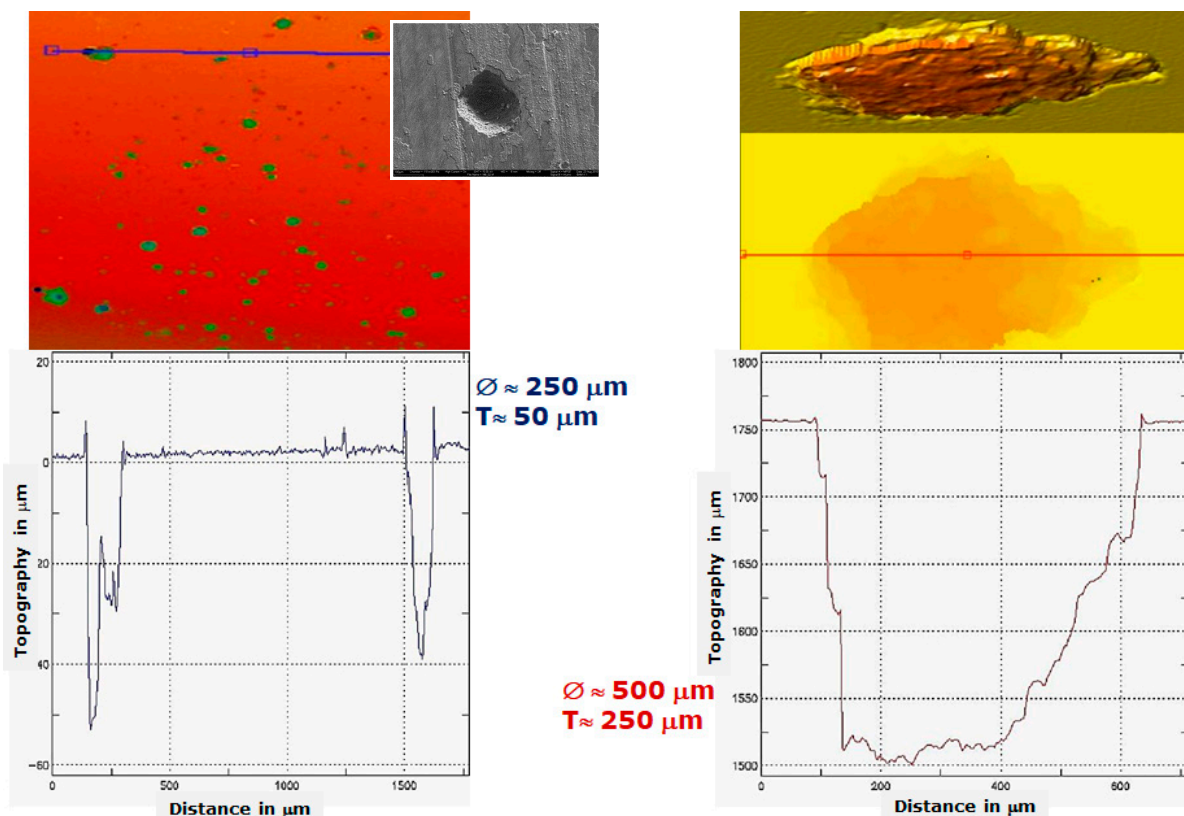


**Figure 11.** Micrograph and optical measurement of pit and pit intrusion depth of X5CrNiCuNb16-4.

Since local corrosion is a highly statistical phenomenon it is not predictable. Hence, it is not possible to give reliable corrosion rates and lifetime predictions regarding pit corrosion in CCS technology [104].



### 3.4. Statistical Approach in Corrosion Fatigue

Specimens were tested at different stress levels each (the string of pearls method). Logarithms of stress amplitude  $\sigma_a$  and the number of cycles to failure  $N_f$  were used in the following method of linear regression analysis assuming a logarithmic normal distribution of the number of cycles to failure  $N_f$  [36,52]. As a result, the scatter bands for the survival probabilities PS are parallel to the PS = 50% straight (regression) line according to:

- $\log(\sigma_a)$ : Logarithm of stress amplitude  $\sigma_a$ , independent (error-free) variable x;
- $\log(N_f)$ : Logarithm of cycles to failure  $N_f$ , dependent variable y (inaccurate);
- $m$ : Estimate for the slope of the regression line;
- $b$ : Estimate for the intercept of the regression line;
- $t_X$ : One-sided barrier of standard normal distribution for  $P_S = x \%$ ;
- $s_N$ : Standard error of the estimate of  $N$ ;
- $P_S$ : Probability of survival.

Therefore, Equation (10) of the S-N curve follows:

$$\log(N_f) = m \log(\sigma_a) + b + t_X s_N \quad (10)$$

respectively

$$\log(\sigma_a) = \frac{\log(N_f) - b - t_X s_N}{m}$$

The important *standard error*  $s_N$  of the regression calculation is determined from the mean square deviation of each value of the regression line (Equation (11)). The *residual variance*  $s_N^2$  reveals the scatter which cannot be explained by regression:

$$s_N = \sqrt{\frac{\sum_{i=1}^n \{\log(N_i) - b - m \log(\sigma_{a,i})\}^2}{n - 2}} \quad (11)$$

The linear regression was calculated according to Equation (12) as follows:

$$N_{50} = N_A \cdot \left(\frac{S_a}{S_A}\right)^{-k} \quad \text{for } S_a \geq S_A \quad (12)$$

given:

- $N_{50}$  50% probability cycle value;
- $N_A$  reference cycle value;
- $S_A$  reference stress value;
- $S_a$  selected stress value.

The scatter range  $T_N$  is the quotient between the probability cycle value of 10% and 90% (Equation (13)):

$$T_N = 1 : \frac{\log N_{90}}{\log N_{10}} \quad (13)$$

given:

- $N_{90}$  90% probability cycle value;
- $N_{10}$  10% probability cycle value;
- $T_N$  scatter range.

The  $R^2$  value varies from 0 to 1. The higher number indicates higher coherence and statistical certainty. The  $R^2$  value is unusually high (0,99 therefore, very close to 1) possibly due to the scarce dataset or the same fatigue mechanism.

### 3.5. Corrosion Fatigue of X46Cr13 (Air: $\sigma_{ts} = 680$ MPa, $\sigma_y = 345$ MPa, Fatigue Limit: 260 MPa)

Data regarding corrosion fatigue of X46Cr13 was mainly compiled from references: [35,36].



Unlike fatigue tests in air results obtained in geothermal environment does not show in a distinguished fatigue limit. The S-N curve from tests conducted in CO<sub>2</sub>-saturated saline aquifer at 60 °C decreases continuously for X46Cr13 (soft annealed microstructure = ferritic matrix with coagulated cementite,  $\sigma_{ts\text{air}} \cong 680$  MPa,  $\sigma_{y\text{air}} \cong 345$  MPa) [35,36] (Figure 12). The endurance-limit in air ( $\sigma_{ee} = 262$  MPa, Equation (14)) is represented by three run-outs at stress amplitudes: 260, 280, and 288 MPa [35]:

$$\sigma_{ee} = 0.2 (\sigma_y + \sigma_{ts}) + 57 \quad (14)$$

- $\sigma_{ee}$ : Estimated endurance limit in air from the yield and tensile strength in MPa;
- $\sigma_y$ : Yield strength in MPa;
- $\sigma_{ts}$ : Tensile strength in MPa.

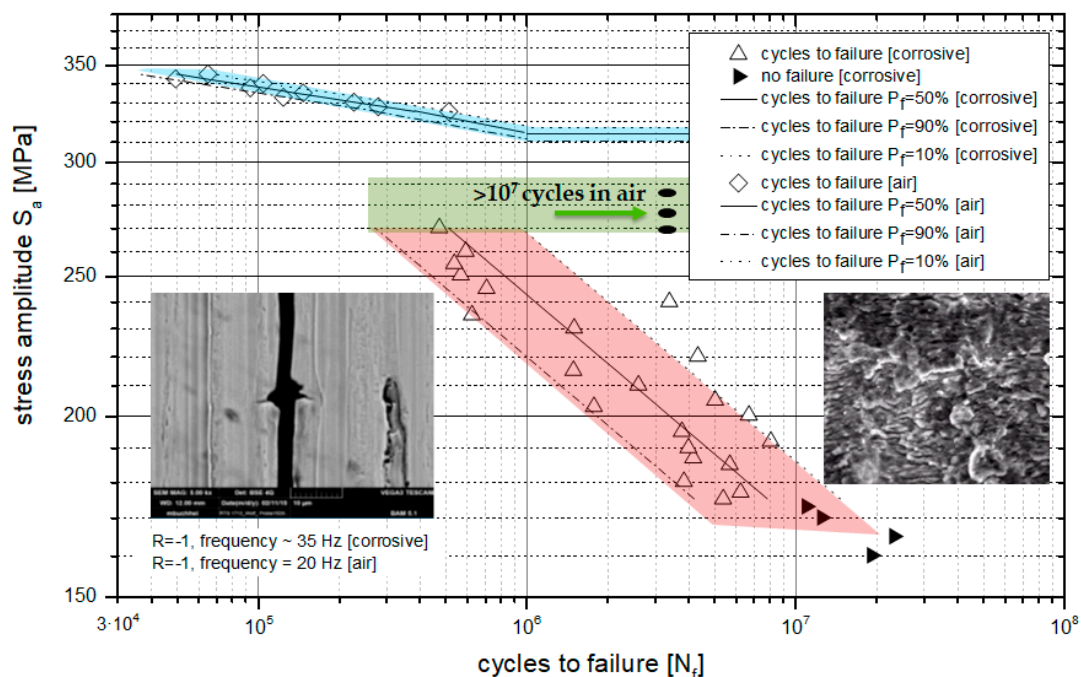


**Figure 12.** S-N curve of X46Cr13 at  $R = -1$ , frequency 30 Hz: Corrosion fatigue compared to the endurance limit in air, fatigue crack, pits, and striations on the fatigue fracture surface.

The influence of corrosion significantly decreases the fatigue life represented by the comparatively steep slope of the S-N curve that is described by  $k = 6.321$ . After 210 h of exposure to CO<sub>2</sub>-saturated geothermal brine ( $21 \times 10^6$  cycles) at 60 °C, the endurable stress amplitude is ca. 160 MPa and thus only 60% of the fatigue limit in air (ca. 260 MPa, Figure 12) [35,36,106,113].

Mostly cracks are associated with rather small pits (diameter  $\ll 0.1$  mm) in the sample middle section with the highest effective stress. Larger corroded areas ( $>0.5$  mm) located in the peripheral section of the specimens reveal only a few cracks (Figure 12). One or more surface cracks developed independently of the stress amplitude  $S_a$  between  $S_a = 187$  and 255 MPa [36]. Cracks initiated from the shallow pit corrosion are predominantly dendritic and single when initiated from small pits [35].

Crack propagation and finally the corrosion fatigue failure of X46Cr13 is related to more than one initial micro crack (100  $\mu\text{m}$  width and 50  $\mu\text{m}$  depth) at stress amplitude  $\sigma_a = 220$  MPa and 4 to 5 cracks of various sizes at  $S_a = 173$  and 230 MPa. At stress amplitudes  $S_a < 230$  MPa, initial crack regions are associated with pits. Exceeding  $\sigma_a > 230$  MPa, only mechanical stress causes failure. Although striations are selectively present in all samples (Figure 12) fatigue cracking cannot clearly be distinguished from corrosion fatigue in the passive state (passivated crack flanks reducing corrosion fatigue).

### 3.6. Corrosion Fatigue of X5CrNiCuNb16-4 (Air: Fatigue Limit: 620 MPa)

Data regarding corrosion fatigue of X5CrNiCuNb16-4 was mainly compiled from references: [79,90,91,99,106,113,115].

The endurance limit in a corrosive environment of X5CrNiCuNb16-4 is lower than in air (620 MPa) by 60% [116] revealing a much steeper fatigue limit line [98,99,108]. First, results showed that the S-N curve did not reveal the expected fatigue strength and non-linear very steep slopes of the possible fatigue strength for finite life ( $k = 3.59$ ,  $T_N = 1:34$ ,  $r^2 = 0.33$ , max.  $N_f = 10 \times 10^7$ ) at  $S_a = 150$  MPa [79,99,100]. New results showed a smaller scatter but also a steep slope of the fatigue limit line pointing to a fast degradation and low maximum  $N_f$  ( $10 \times 10^7$  at  $S_a = 130$  MPa) (Figure 13) [103,106,108].

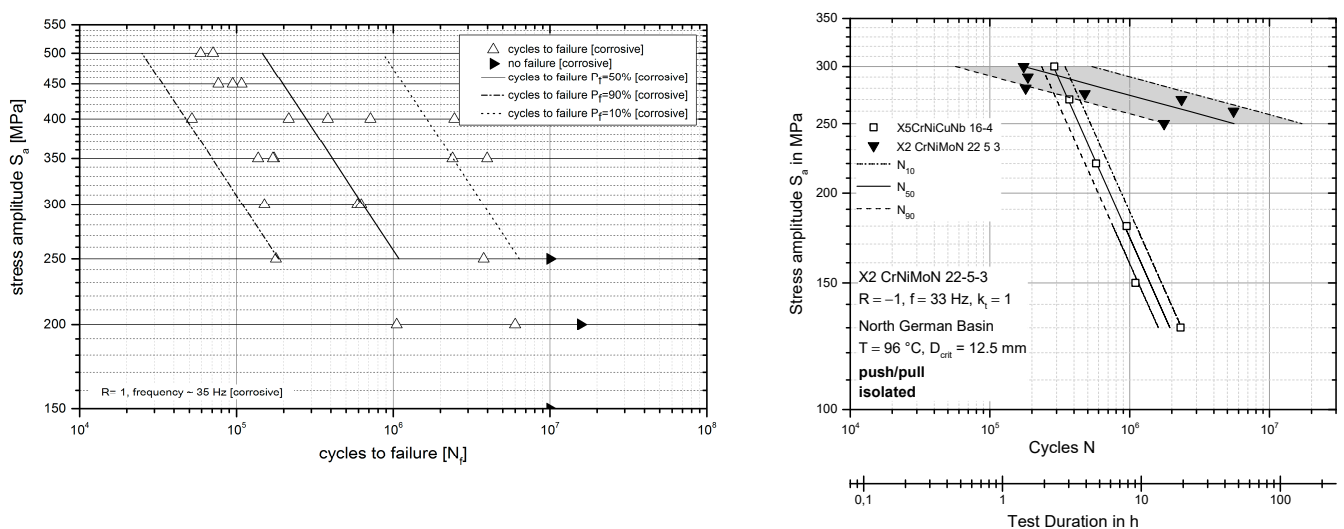


**Figure 13.** S-N curve and crack formation on the 1.4542 first and second set of experiments exposed to saline aquifer water and technical CO<sub>2</sub>. Comparison results for 1.4462 are given.

Pits are a source of multiple cracks [113]. Local corrosion is enhanced by the mechanical load increasing the local microstructural boundary energy of X5CrNiCuNb16-4 due to the local lattice mismatch [36], increased dislocation number, grain boundaries, precipitation phase boundaries, and carbides [36], as well as the presence of chlorides [46].

The specimen with a presumably short number of cycles to failure typically consisted of non-metallic inclusions communized with  $\delta$ -ferrite [99,100,108,113]. Moreover, aluminum was in specific samples but could not be identified as a significant reason for the low number of cycles and early failure [90]. Early failure could not significantly be associated with heterogeneously distributed aluminum [90] and other microstructural impurities, artificial aquifer water [106,107,113], stress amplitude, number of striations or thickness of the corrosion layer.

A cathodic potential clearly enhances the corrosion fatigue life expectancy by a factor of 20 to 70 ( $U_{SHE} = -400$  to  $-150$  mV) [116]. The specimen degrades slower at low potentials and faster at high potentials. The fatigue life expectancy (number of cycles to failure) is increased with the decreasing potential considering the drawback that a cathodic potential discharges H<sub>2</sub> from the specimen's surface and accelerates embrittlement of the alloy, which causes earlier and unpredicted failure [116].

### 3.7. Corrosion Fatigue of X2CrNiMo22-5-3 (Air: Fatigue Limit: 485 MPa)

Data regarding corrosion fatigue of X2CrNiMo22-5-3 was mainly compiled from references: [52,79,90,92,100,106,109].

In air, the fatigue limit of duplex stainless steel X2CrNiMoN22-5-3 is 485 MPa ( $P_f = 50\%$ , push/pull,  $N_f = 10^7$  cycles) [33–35]. The steep slope of the S-N curve ( $k = 8.78$ ) typical in a corrosive environment reveals a low scatter range  $T_N$  (1:1.35), therefore generally

indicating the same failure mechanism. The maximum number of cycles of ( $9.2 \times 10^6$ ) in a corrosive environment at a free corrosion potential (resting potential) was determined at a stress amplitude of 240 MPa.

Failure is always characterized by an abrupt drop of potential, but here, at approximately 10 min prior to the potential, failure began to decrease steadily indicating an upcoming failure [82].

### 3.7.1. Influence of Machine Insulation

Since electric insulation was found to affect the corrosion fatigue behavior of the steel, the subsystem specimen/corrosion chamber were electrically grounded and shielded [81]. (Note that grounding only does not supply reliable corrosion fatigue data due to the insufficient electric shielding of the specimen).

An insulated setup is characterized by a higher S-N coefficient of  $k = 4.7$  in comparison to an uninsulated setup ( $k = 8.78$ ) (Figure 14) [52], which depends on the more cathodic electrochemical potential. Starting from the same value at 400 MPa, the two S-N curves diverge as the stress amplitude decreases. Insulation shifts the potential to a more noble regime. At the same time, the range reduces to ca.  $U_{SHE} = -5$  to  $-65$  mV. Failure is also presaged by a distinct potential drop.

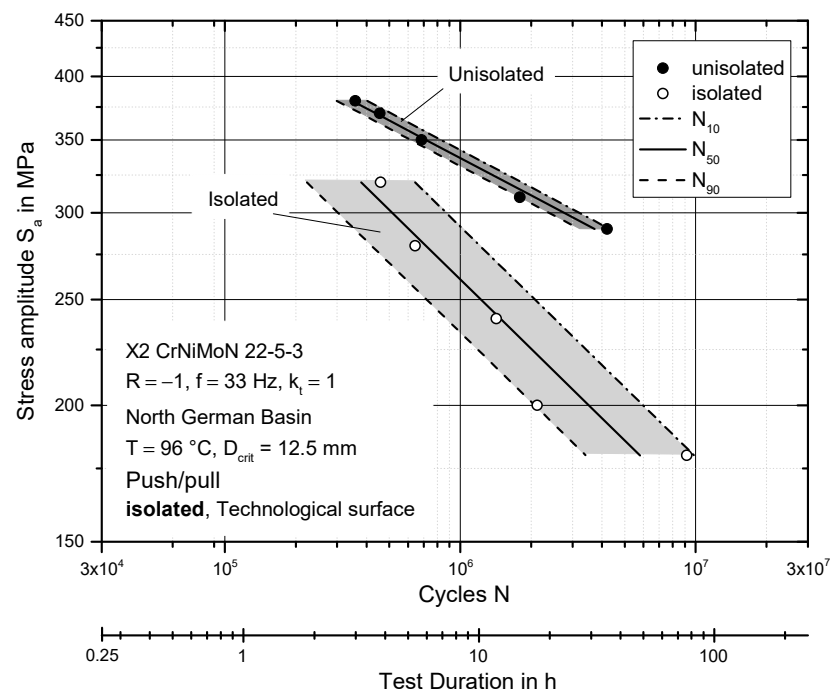


**Figure 14.** Corrosion fatigue X2CrNiMoN22-5-3. S-N curves, uninsulated and insulated experimental setup.

### 3.7.2. Influence of Electrochemical Potential

When a critical potential is applied the corrosion effects can be repressed [52,90]. The application of the critical cathodic potential at a stress amplitude of 275 MPa increases the number of cycles compared to the free corrosion potential. The initiation of local corrosion is suppressed that otherwise initiates crack formation and therefore increases fatigue life. The cathodic potential at 275 MPa increases the number of cycles from  $4.7 \times 10^5$  (free potential at: ca.  $-3$  mV) to  $2.6 \times 10^6$  ( $-150$  mV) up to  $5.4 \times 10^6$  at  $-300$  mV and  $10^7$  cycles at a potential of  $-450$  to  $-900$  mV. As a back draw, hydrogen evolves from the specimen's surface at very low potentials [90] (an anodic potential causes severe pit formation and therefore a more rapid failure of the specimen).

### 3.7.3. Influence of Load Type

The superior corrosion fatigue resistance in a geothermal environment under the rotation bending load is significant by the factor 1.11–1.25 in the cycle range  $10^5$  to  $10^6$  [90]. The initially better corrosion fatigue properties under the rotation bending load (higher stress amplitudes at a certain number of failure) become less significant with the increasing number of cycles. The S-N 50% probability graphs converge at approximately  $3.5 \times 10^6$  cycles (30 h of cyclic loading), eliminating the advantage of the rotation bending load (slope factors of rotating bending  $k = 8.2$  and push/pull  $k = 19$ ). The greater negative slope coefficient achieved for rotation bending experiments describes the higher rate of alloy degradation and therefore greater susceptibility to the corrosive attack, especially after high cycle numbers and therefore long exposure to a corrosive environment.

### 3.7.4. Influence of Surface Conditions

Data regarding the influence of surface conditions on the corrosion fatigue of X2CrNiMo22-5-3 was mainly compiled from references: [52,91,92,109].

The surface roughness influences the corrosion fatigue behavior of the duplex steel significantly (note that there is no influence on the corrosion fatigue behavior within one experimental series). The line of regression for technical surfaces has a greater negative slope (steeper) ( $k = 8.78$ ) than for polished surfaces ( $k = 19.006$ ). (Note that the lines of regression with a small number of  $k$  decline greater than those with large numbers of  $k$  (Figure 15)). Rather, the low scatter ranges (technical surface: TN = 1:1.35, polished surface: TN = 1:1.95) indicate no change in failure mechanism.

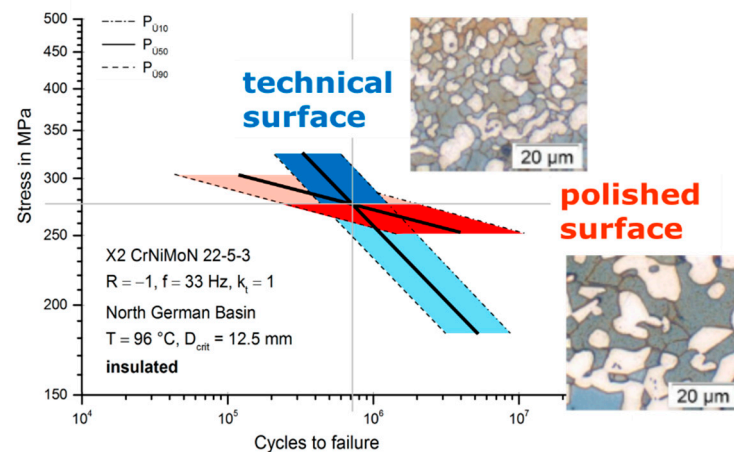


**Figure 15.** Influence of surface finish quality and local corrosion initiation on CF, S-N curves, and insulated test setup. (Top right): Turned, (bottom right): Polished.

As discussed in detail [92,109], a polished surface finish (approximate  $R_z = 1.4$ – $1.59 \mu\text{m}$ ) inhibits degradation compared to the turned surface finishes (approximate  $R_z = 3.2 \mu\text{m}$ ). The specimen with technical surfaces ( $R_z = 2.6$ – $4.6$ ) tested at stress amplitudes above 275 MPa ( $9 \times 10^5$  cycles) ( $P_{50\%}$  at  $S_a$  300 MPa =  $5 \times 10^5$ ) reveal a higher life expectancy than the specimen with polished surfaces ( $P_{50\%}$  at  $S_a$  300 MPa =  $1.5 \times 10^5$ ) (Figure 15). The life expectancy for polished surfaces, however, increases with the test duration and decreasing stress amplitude. Smoother polished surfaces provide little to no additional stress concentration associated with the base region of micro-notches and inhibit crack initiation and early failure [52].

## 4. Discussion

In general, a higher Ni and Cr content in the heat treated steels improve the corrosion resistance [22,27], also proven by the steels investigated in this study. Moreover, the intermediate heat treatment protocols for steels with continuous martensitic microstructures are

favorable in terms of good corrosion resistance and are widely discussed before [9,17]. The corrosion rate is more susceptible to the heat treatment at 100 bar than at ambient pressure. Therefore, the heat treatment is less significant compared to the chromium content and atmosphere. Hardening or hardening and tempering coupons are promising at ambient pressure with regards to low surface corrosion rates. Considering surface corrosion only, at 100 bar the martensitic microstructure (hardened and tempered at 650 °C for the supercritical phase: <0.001 mm/year) is superior in water saturated supercritical CO<sub>2</sub>. However, in the CO<sub>2</sub> saturated aquifer, the water normalized ferritic-perlitic microstructure is sufficiently resistant against corrosion (ca. 0.004 mm/year) [98,104].

Here, we will briefly discuss specifically picked topics that we find most interesting.

#### 4.1. Precipitation of Corrosion Scales in a Geothermal Environment

High alloyed steels exposed to water saturated CO<sub>2</sub> show little dependence on the exposure time or heat treatment. Corrosion rates remain nearly constant at approximately 0.004 (X5CrNiCuNb16-4)-0.4 (X46Cr13) mm/year. The sufficiently thick carbonate layer acts as a diffusion barrier passivating the steel [36,89,90,99,104,113,115,116].

Heterogeneous carbonate layers are formed in a CO<sub>2</sub>-saturated saline aquifer and cover the specimens' surface and pits because carbonic acid forms, which reduces the siderite FeCO<sub>3</sub>-solubility in CO<sub>2</sub>-containing water with a rather low pH [24]. Main phases at ambient pressure are: Siderite FeCO<sub>3</sub> and cementite Fe<sub>3</sub>C. Moreover, goethite α-FeOOH at 100 bar and mackinawite FeS, akaganeite Fe<sub>8</sub>O<sub>8</sub>(OH)<sub>8</sub>Cl<sub>1.34</sub>, and spinel-phases of various compositions [98,99,103,113].

The corrosion rates first increase in a CO<sub>2</sub>-saturated saline aquifer, then passivate resulting in decreasing corrosion rates but later the rates increase again (ca. 0.004 to 0.014 mm/year for X5CrNiCuNb16-4). The passivating layer breaks down and gaseous CO<sub>3</sub><sup>2-</sup> and O<sub>2</sub>-species diffuse into the metal and iron diffuses towards the surface. Here, siderite FeCO<sub>3</sub> layers form (Figure 16) [9,15,17,36,99,113]. Due to the fact that the larger areas of the corrosion layer locally detach, a fresh surface is exposed to the brine and corrosion reactions accelerated [113].

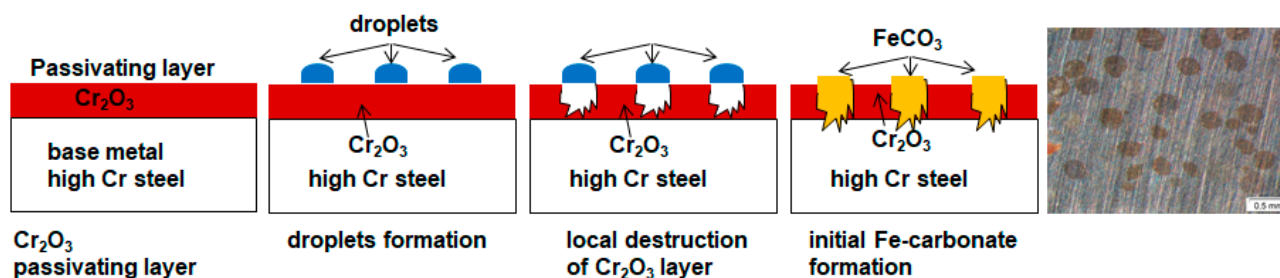


**Figure 16.** Schematic drawing of the precipitation of the corrosion layer on X5CrNiCuNb16-4 (1.4542) and an example of sample surfaces after 8000 h of exposure to water saturated supercritical CO<sub>2</sub>.

However, X5CrNiCuNb16-4 shows an unusual corrosion behavior forming homogeneous ellipsoids on the surfaces (Figures 12 and 16 (leopard shaped)). The corrosion layer reveals inhomogeneously thick carbonate corrosion products on the surface such as siderite FeCO<sub>3</sub>, goethite FeOOH, and carbides, mainly Fe<sub>3</sub>C. The center of the typical ellipsoids at exposure greater than 4000 h reveals mainly hematite Fe<sub>2</sub>O<sub>3</sub> but also iron sulfate FeSO<sub>4</sub>, siderite FeCO<sub>3</sub>, and goethite FeOOH—the latter also after corrosion fatigue tests.

Corrosion ellipsoids may form since carbides are distributed heterogeneously within the microstructure and these are more susceptible to initial corrosion [34] steels, which are locally depassivated [98].

Another likely explanation depends on water solubility, pressure, and temperature [98]. Generally, the solubility of water increases with temperature. However, under pressure, the solubility of water decreases from 0 to 50 bar and then increases again slightly [31]. In water saturated supercritical CO<sub>2</sub> at 100 bar and 60 °C, the metal surface is



wetted due to the decreasing water solubility in the supercritical CO<sub>2</sub>. Consequently, small and very thin “leopard”-shaped droplets form and thin corrosion layers grow. Due to the oxygen content (Figure 12), these are most likely iron carbonate or iron hydroxide.

Consolidating droplets form small pits around the former droplet and corrosion processes are enhanced at this distinct multiphase boundary (water, metal, supercritical CO<sub>2</sub>). Since small droplets are formed much faster, the consolidated water diffuses back into the supercritical CO<sub>2</sub>. As a consequence, the area of consolidated droplets reduces inwards with the sulphates (FeSO<sub>4</sub>) found in the outer and hematite (Fe<sub>2</sub>O<sub>3</sub>) in the centered areas (Figure 12) [98].

#### 4.2. Influence of Austenitizing

Results from the DoE analysis after Klein [117] prove that the surface corrosion resistance is dependent only on the austenitizing time, but neither the austenitizing temperature nor the carbon content of the base material [17] (Figure 17). The carbon content shows the largest impact on the local corrosion but still no significant dependence on the local corrosion behavior [103].

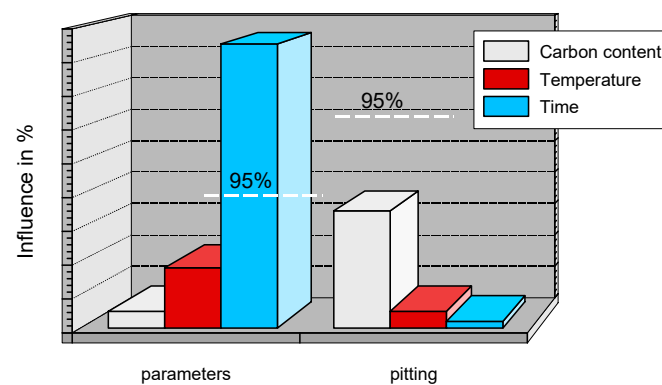


**Figure 17.** The impact of the experimental parameters on the corrosion rate after 4000 h of exposure time combined with confidence intervals.

Generally, martensitic microstructures are highly corrosive (up to two orders of magnitude higher than ferritic or ferritic-bainitic microstructures) since grain boundaries are more reactive [25,118]. However, increasing the austenitizing temperature lowers the pitting potential of lean high alloyed steels [24,28,82] with a maximum improvement by annealing at 1200 °C [24]. Since carbides dissolve at high annealing temperatures the corrosion resistance of martensitic stainless steels with 13% Cr increases at higher austenitizing temperatures (980–1050 °C) [25,30,91]. (Note that Cr-rich M<sub>23</sub>C<sub>6</sub> and M<sub>7</sub>C<sub>3</sub> carbides generally increase the mechanical properties due to secondary hardening [30], but reduce the resistance of a passivating film and enhance pitting [82]). However, at the beginning, the corrosion rates of X46Cr13 and X20Cr13 are significantly higher after austenitizing at higher temperatures and longer holding times, but after 4000 h of exposure to the CCS environment the corrosion rates are of not much difference. Most likely the advantageous carbide dissolution at high austenitizing temperatures is not the driving corrosion force and the grain boundaries are corrosively attacked. Diffusion processes are slowed down with the increasing thickness of the growing corrosion layer. Additionally, shorter austenitizing at a low temperature limits the grain growth by not allowing for equilibration. The slow grain growth leads to coarse grain sizes resulting in lower corrosion rates. Moreover, the retained austenite at a low austenitizing temperature may be beneficial against pitting of 13%-chromium steels (13CrNiMo) [26]. However, in a geothermal environment, austenitizing does not influence the corrosion behavior after long exposure times (Figure 13).



#### 4.3. Crack Initiation and Corrosion Fatigue Failure of High Alloyed Steels X46Cr13 and X5CrNiCuNb16-4

The deterioration of grain boundaries and pit formation initiate crack formation thus failure of high alloyed steels under cyclic load in a (CO<sub>2</sub>-saturated) corrosive geothermal environment [32–34,36,99,113].

Pits on stainless steels form due to chemical reactions, local changes of lattice energy within the steel's surface, and mechanical load [9,15]. During cyclic stress-strain loading, plastic deformation is a reason for strain and work hardening effects increasing the grain/phase boundary energy at dual or triple points of grain/phase boundaries, residual perlite grains, and more likely carbides [34]. This local lattice mismatch initiates pit -, selective-, and intergranular corrosion, as well as crack formation [33] and accelerates crack propagation [32,34].

At the beginning, the pits form grain and phase boundaries catalyzing corrosion reactions. In geothermal water with high chloride concentrations, the phases arrange at equilibrium and dissolve an outer metastable oxide/hydroxide film before siderite then precipitate [9,15] despite a passivating inner chromium oxide film [31,53]. Mu et al. [6] illustrated that siderite forms when carbonate ions absorb into the base material at the hydroxide/brine interface and combine with oxygen vacancies (cation/oxygen vacancy pairs of Mott-Schottky-type). At the hydroxide/brine interface, oxygen vacancies and additional carbonate ions form excess cation vacancies. These travel to the hydroxide/siderite interface, consolidate, and condense to form larger vacancy areas. As a consequence, the siderite and hydroxide film detach, enhancing pitting and lateral surface degradation [6,36].

A possible crack initiation model was presented by Han et al. [37] and modified by Pfennig et al. [17,35,36,99,113] (Figure 18): Initially, pits catalyze corrosion on steels exposed to CO<sub>2</sub>-environment [15,17,29] and siderite FeCO<sub>3</sub> [3,38] precipitates (a). Anodic iron dissolution forms transient Fe(OH)<sub>2</sub> [6,30] (grey area in: a) The pH rises locally at the hydroxide film and a thin ferrous carbonate layer precipitates internally and externally (a and b) (Equations (1)–(6)) [15,29,37]. Both corrosion layers grow with regards to carbon and oxygen partial pressures (b). When the ferrous hydroxide film (c) is locally damaged (either mechanically or chemically) the non-protective porous ferrous carbonate film is exposed to the brine (local low pH). It dissolves and depassivates the steel (d) intensifying local surface degradation. Oxygen vacancies consolidate and condense at the hydroxide/brine interface resulting in the lateral spallation of the siderite from the hydroxide aligned to the mechanical stress applied (e). The remaining film is dissipated by the flowing brine inducing further pit enlargement, since the newly exposed surface reactions will start repeatedly from the top (f). Concurrently, cracks initiate and propagate due to the cyclic load and additional forces at the pit bottom, where the stress concentration and plastic deformation produce slip bands [26] at the crack flanks. Newly formed slip bands are susceptible to corrosive reactions as explained and once wetted the corrosion steps repeat within the crack itself.

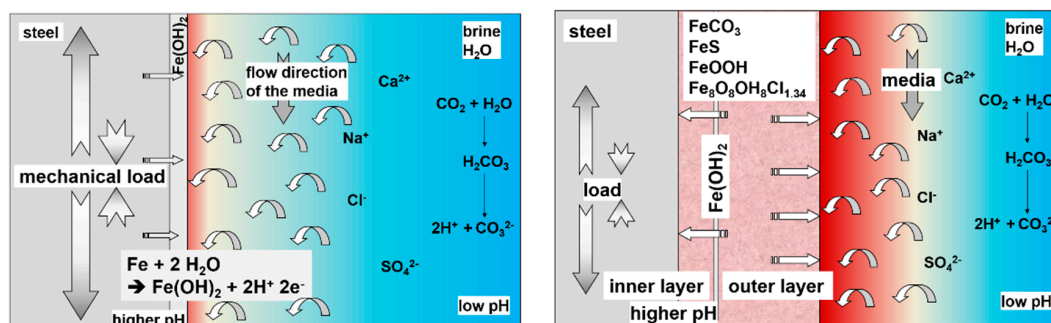


Figure 18. Cont.

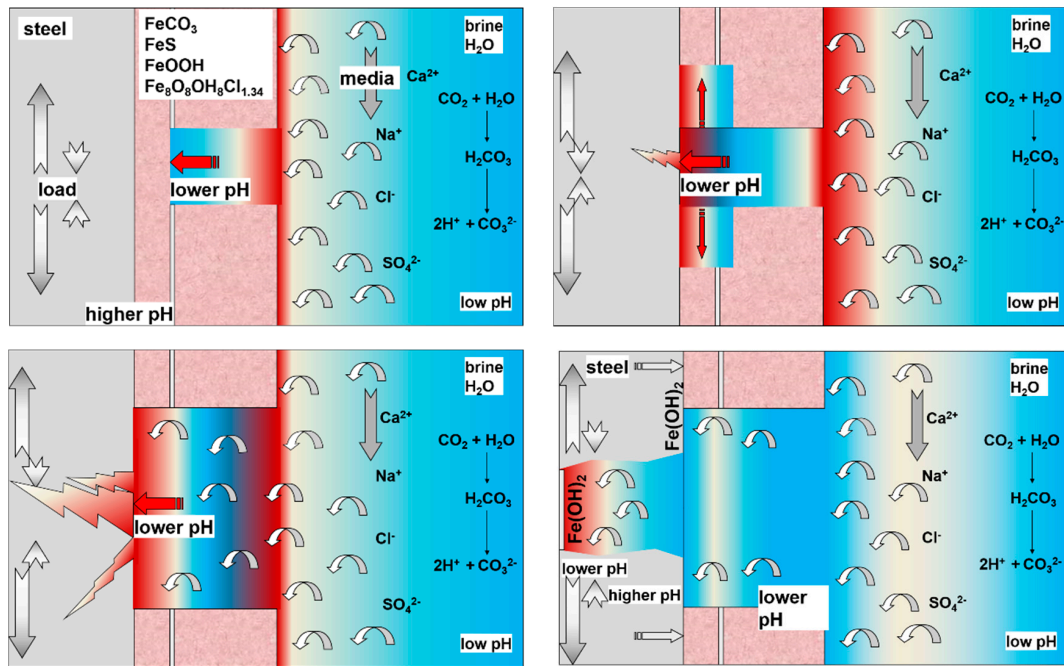


Figure 18. Schematic crack initiation model modified by Han et al. [37].

#### 4.4. Influence of Surface Quality on the Corrosion Fatigue of Duplex Stainless Steel X2CrNiMoN22-5-3

Generally, technical surfaces of duplex stainless steel X2CrNiMoN22-5-3 (1.4462, equilibrium at 98 °C in a corrosive environment of the Northern German Basin (NGB) at 275 MPa) reveal good corrosion fatigue resistance in a CCS or geothermal environment at low stress amplitudes. Note: at  $S_a > 270$  MPa, technical surfaces (average surface roughness of 3.2  $\mu m$ ) the fatigue life succeeds that of polished surfaces (average surface roughness of 1.59  $\mu m$ ). At  $S_a < 270$  MPa, polished surfaces succeed technical surfaces (Figures 15 and 19) [81–84].

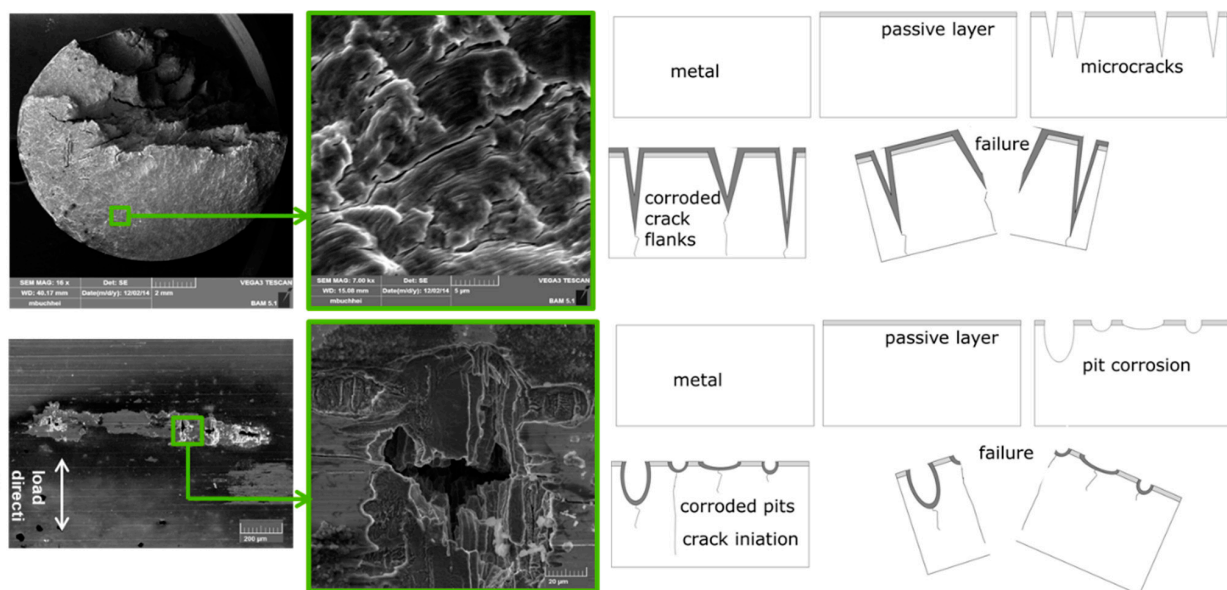
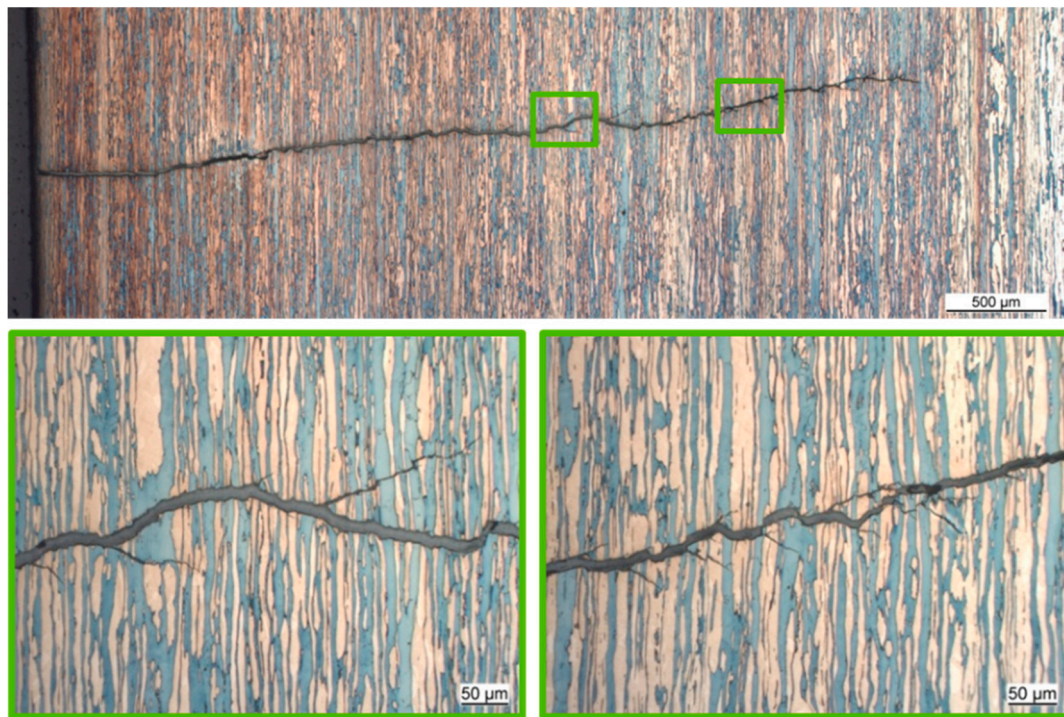


Figure 19. Schematic S-N curves of 1.4462 X2CrNiMoN22-5-3 in air and the corrosive media Northern German Basin at 98 °C after machine turning (technical surface) and polishing (polished surface).

Cracks usually propagate perpendicular to the laminar duplex structure (Figure 20). Sanjuro et al. [82] stated that residual stress only contributes 10% to the enhanced corrosion fatigue behavior. Mostly surface finishing accompanied with the removal of surface stress raisers contribute. However, the specimen with technical surfaces plastically deform and harden during machining. The influence of this residual compressive stress might weigh higher than the increased surface roughness and is responsible for the high fatigue life expectancy at amplitudes above 275 MPa [109].



**Figure 20.** Microsection of macro crack with significant residual surface opening. Etchant: Beraha II (top) [93]. Microsections of major crack initiation (left) and major crack termination zone (right) (380 MPa;  $0.36 \times 10^6$  cycles).

Another explanation is related to a changing mechanism of crack growth depending on the stress amplitude (note: At 275 MPa, the overlapping regression lines prove that the surface condition does not influence the corrosion fatigue behavior).

At  $S_a > 275$  MPa, the overall tensile stress in the specimen during push-pull loading enhances the micro crack formation (Figure 20). During cyclic loading the crack constantly opens and closes exposing the (newly formed) crack flanks to the geothermal media. As a consequence of the corrosive reactions described earlier [26,81,105], siderite precipitates and segregates. Since the strain of the corrosion layer and base metal do not match further the mechanical stress causes crack propagation until failure. High endurance limits are generally found for high strength material and because technical surfaces may reveal increased strength from compressive stress, the number of cycles to fatigue is higher for technical surfaces at  $S_a > 275$  MPa [109].

At  $S_a < 275$  MPa, pit corrosion is responsible for crack formation. During exposure to the mechanical load and corrosive environment pits grow to a critical size and due to a notch effect, the fatigue cracks form (Figure 19) [68]. Local corrosion is a reason for micro crack initiation at  $S_a < 270$  MPa and therefore, polished surfaces suppressing pit formation are a reason for higher numbers of cycles to failure [93,109].

Generally, the surface roughness may be neglected for small stress amplitudes where pitting is the driving force for crack initiation. At high stress amplitudes, mechanically induced micro cracks are responsible for crack initiation and propagation.



#### 4.5. Failure of Duplex Stainless Steel X2CrNiMoN22-5-3 in a Geothermal Environment

When X2CrNiMoN22-5-3 is tested under axial push-pull load, the crack path is normal to the load direction [93]. Cracks propagate predominantly perpendicular to the lamellar austenitic as well as ferritic phases [91,93] (Figure 20, top).

Linear crack propagation leaves a 30  $\mu\text{m}$  residual crack width. Multiple small secondary micro cracks ca. 3 mm below the sample surface (Figures 20 and 21) are associated with pits and disappear soon after initiation. The remaining pits form cavities.

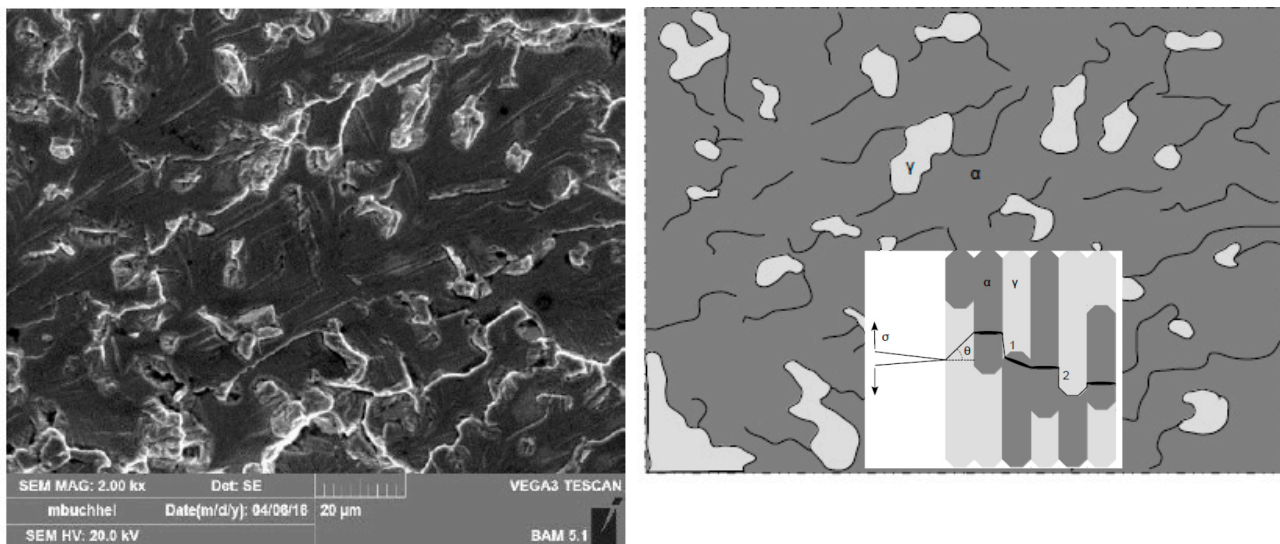


**Figure 21.** Left: Cross section through the corrosion pit. Etchant: Beraha II. Right: Schematic drawing showing the preferred deterioration of the austenitic phase ( $\gamma$ ).

Figures 20 and 21 proof that mainly the austenitic phase corrodes at crack flanks and within cavities, whereas the ferritic phase remains uncorroded since the electric potential dominates [91,93]. Due to higher contents of molybdenum, chromium, and nitrogen, elements known to improve corrosion resistance, the pitting resistance equivalent number (PREN) is lower for the austenitic 32.37 than the ferritic phase [91,93] resulting in a lower corrosion resistance of the austenitic phase (total: 37.39). (Note that a high PREN = high corrosion resistant for high alloyed steels). Moreover, due to its face cubic centered (FCC) structure, the large octahedral interstitial sites of the austenitic phase (mean diameter ca. 0.41 R (R = average atomic radius)) can incorporate more corrosive elements than the body cubic centered (BCC) ferritic phase with only small octahedral interstitial sites (ca. 0.20  $\mu\text{m}$ ). Since diffusion is enhanced in structures with a large voids intrusion of, e.g., chlorides from the brine and therefore, pitting is preferential in the austenitic phase or austenite-ferrite phase boundary.

The initiation of corrosion fatigue failure in the passive state may be first derived from local corrosion effects and secondly from the decay of passivation [91,93] (Figure 22): 1. Pitting causes the formation of initial micro cracks. The area of micro cracks is depassivated followed by crack propagation when the stress rises above a critical level. 2. The passivation layer is locally destroyed and since the mechanical axial push-pull load develop a slip band that grows at the metal surface the enlarged material surface is exposed to the corrosive environment. Pits now originate easily and lead to micro crack formation. Both mechanisms result in crack formation that degrades the crack flanks and consequently lead to failure (Figure 21, right and Figure 22, right). Environmentally induced cracks in railway axels exposed to artificial rainwater tend to initiate from localized corrosion pits for smooth surface specimens [50], but Hu et al. [50] did not find that corrosion pits are observed at the crack nucleation sites for scratched specimens. Therefore, the surface condition also

influences crack nucleation with or without pitting. Intergranular cracking was stated for both conditions [50], while the duplex steel also shows transgranular cracking.

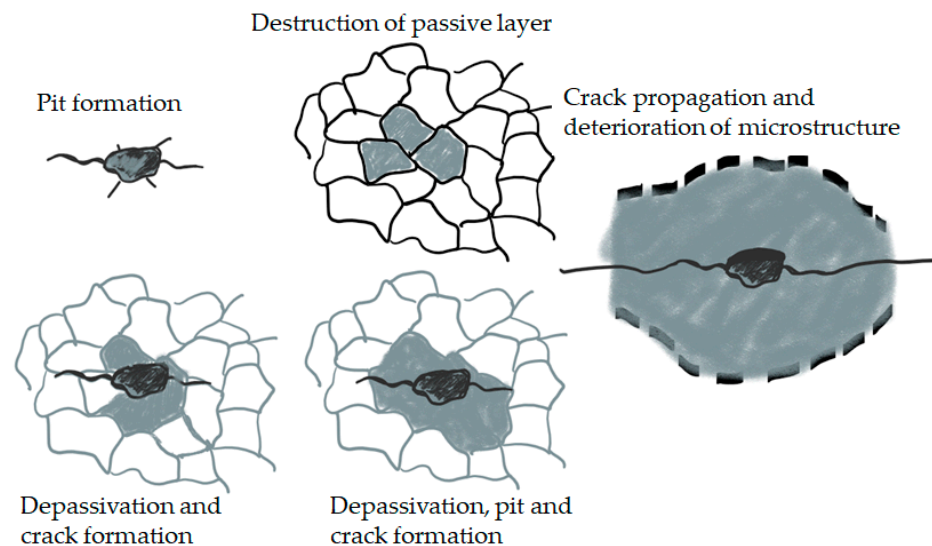


**Figure 22.** Schematic failure routes during corrosion fatigue. Left: Pitting results in depassivation and crack formation. Middle: Depassivation leads to pitting and crack formation. Right: Crack formation and degradation of the microstructure within the crack flank region.

## 5. Conclusions

This paper comprises and compares data of previously published work: [9,15,17,35,36,38,52,53,79,89–93,97–100,103–106,108,109,113,115–117].

The corrosion and corrosion fatigue behavior of AISI 420 (X20Cr13, 1.4021), AISI 420C (X46Cr13, 1.4043), No AISI (X35CrMo17, 1.4122), AISI 630 (X5CrNiCuNb 16-4, 1.4542), and AISI A182 F51 (329LN) SAF 2205 (X2 CrNiMoN 22-5-3 (UNS S31803) 1.4462) were tested in the laboratory CO<sub>2</sub>-saturated CCS environment of the onshore saline aquifer (Stuttgart Aquifer and Northern German Basin).

### 5.1. Static Corrosion

1. Corrosion products: The continuous corrosion scale and pits of all steels mainly comprises of FeCO<sub>3</sub> and FeOOH at ambient pressure as well as 100 bar. X5CrNiCuNb 16-4 shows an unusual non-uniform ellipsoidal corrosion layer additionally containing Fe<sub>3</sub>C and in the center Fe<sub>2</sub>O<sub>3</sub> and FeSO<sub>4</sub>.
2. Influence of pressure: After 8000 h of exposure, corrosion rates are generally much lower at 100 bar than at ambient pressure (depending on the atmosphere: (Vapor or liquid) by a factor of ca. 10–80 for 42CrMo4, a factor of ca. 1.5–30 for X46Cr13, a factor of ca. 10–100 for X20Cr13, and a factor of ca. 10 for X35CrMo17-1. (Note that X5CrNiCuNb16-4 shows similar surface corrosion rates in the liquid phase).
3. Influence of atmosphere: Generally, the corrosion rates at ambient pressure are higher in the vapor phase, at 100 bar higher corrosion rates are found in the liquid phase. Independent of pressure the higher number of pits was found for the liquid phase.
4. Influence of alloy composition: Higher chromium content increases surface corrosion resistance, while carbon has no significant influence (ambient pressure, vapor phase: 0.8 mm/year for 42CrMo4 (1% Cr), 0.3 mm/year for X46Cr13 (13% Cr), 0.3 mm/year for X20Cr13 (13% Cr), 0.1 mm/year for X35CrMo17-1 (17% Cr), and 0.01 mm/year for X5CrNiCuNb16-4 (16% Cr)). However, the local corrosion behavior of X35CrMo17-1 and X5CrNiCuNb16-4 compares to the less costly X20Cr13 and X46Cr13. At 100 bar and 8000 h of exposure with no significant regard of atmosphere, the highest corrosion rates are 0.01 mm/year for 42CrMo4, X20Cr13 (liquid phase) X46Cr13, and less than 0.01 mm/year for X35CrMo4 and X5CrNiCuNb16-4.

5. Influence of heat treatment: In general, the shorter austenitizing time and lower austenitizing temperature result in better corrosion resistance regarding surface corrosion, but has no significant impact on the number of pit and pit sizes. At 100 bar as well as at ambient pressure and 60 °C, hardening and tempering at low temperatures (600 to 670 °C) for X20Cr13, X46Cr13, and X5CrNiCuNb16-4 result in the lowest corrosion rates and reveal good resistance against local corrosion. Therefore, the best corrosion resistance is achieved by a continuous martensitic microstructure.

## 5.2. Corrosion Fatigue

In general, the fatigue strength of steels in a CCS environment is reduced and no typical endurance limit of S-N curves exists compared to non-corrosive conditions. Primarily, pitting (pit/local corrosion) driven by the formation of carbonic acid, not the mechanical loading, induces crack formation and propagation and therefore, is most likely the cause for failure.

X46Cr13 (air: Endurance limit: 260 MPa). Max. number of cycles to failure is  $1.10 \times 10^7$  at stress amplitude 173

MPa under CCS conditions. Corrosion fatigue in the passive state is assumingly the main cause for failure. Above  $S_a = 170$  MPa, 90% of the specimen has typical multiple cracks that originate from a central 0.2 mm pit. The initial local corrosion initiates cracks that then condition the inter crystalline corrosion.

X5CrNiCuNb16-4 (air: Endurance limit: 620 MPa). Corrosion phenomena are unusual, such as: Elliptic surface pattern, no typical corrosion fatigue limits of S-N plot, high Wöhler-exponent ( $k = 3.5$  and scatter range (TN = 1:34), and very small coefficient of correlation ( $r^2 = 0.33$ ). The max. number of cycles to failure of  $10 \times 10^6$  at  $S_a = 150$  MPa is even lower in a second experimental set ( $10 \times 10^7$  at  $S_a = 130$  MPa). Local corrosion and inclusions at the fracture surface as well as the inter crystalline corrosion of crack flanks during crack propagation lower the number of cycles to failure independent of: Hardness (335 HV10), aquifer water composition, and microstructure.

X2CrNiMoN22-5-3 (air: Endurance limit: 485 MPa): Max. number of cycles for standard duplex stainless steel X2CrNiMoN22-5-3 without insulation of the testing machine is  $4.2 \times 10^6$  at  $S_a = 290$  MPa and  $9.2 \times 10^6$  at  $S_a = 240$  MPa with insulation. Initially, the crack follows a linear path perpendicular to the axial load followed by a delta-like micro crack structure with an overall curved path with considerable horizontal degradation of the austenitic phase only. Crack initiation may be allocated to both: First, early pit formation results in depassivation and then second, local depassivation results in pit formation.

At the critical electrical potential at  $U_{SHE} = -450$  to  $-900$  mV at  $S_a = 275$  MPa, the specimen did not fail ( $10^7$  cycles to failure). However, at low potentials hydrogen evolves to degrading the steel.

Polished surface finishes result in a higher corrosion fatigue life expectancy at medium to low stress amplitudes (long exposure time). At low stress amplitudes, local corrosion is likely to initialize the crack growth. Technical surfaces perform better at high stress amplitudes (and shorter exposure). At high stress amplitudes, micro cracks are the reason for crack propagation and failure.

**Author Contributions:** Conceptualization, A.P. and M.W.; methodology, A.P. and M.W.; software, M.W.; validation, A.P., M.W. and A.K.; formal analysis, A.P. and M.W.; investigation, A.P. and M.W.; resources, A.P., A.K. and M.W.; data curation, A.P. and M.W.; writing—original draft preparation, A.P.; writing—review and editing, A.P.; visualization, A.P.; supervision, A.P. and A.K.; project administration, A.P.; funding acquisition, A.P. All authors have read and agreed to the published version of the manuscript.

**Funding:** This research received no external funding.

**Institutional Review Board Statement:** Not applicable.

**Informed Consent Statement:** Not applicable.



**Conflicts of Interest:** The authors declare no conflict of interest.

## References

1. Thomas, C. *Carbon Dioxide Capture for Storage in Deep Geologic Formations—Results from CO<sub>2</sub> Capture Project*; Elsevier Ltd.: London, UK, 2005; ISBN 0080445748.
2. Broek, M.V.D.; Hoefnagels, R.; Rubin, E.; Turkenburg, W.; Faaij, A. Effects of technological learning on future cost and performance of power plants with CO<sub>2</sub> capture. *Prog. Energy Combust. Sci.* **2009**, *35*, 457–480. [[CrossRef](#)]
3. Nešić, S. Key issues related to modelling of internal corrosion of oil and gas pipelines—A review. *Corros. Sci.* **2007**, *49*, 4308–4338. [[CrossRef](#)]
4. Hurter, S. Impact of Mutual Solubility of H<sub>2</sub>O and CO<sub>2</sub> on Injection Operations for Geological Storage of CO<sub>2</sub>. In Proceedings of the International Conference of the Properties of Water and Steam ICPWS, Berlin, Germany, 8–11 September 2012.
5. Zhang, L.; Yang, J.; Sun, J.S.; Lu, M. Effect of pressure on wet H<sub>2</sub>S/CO<sub>2</sub> corrosion of pipeline steel. No. 09565. In Proceedings of the NACE Corrosion 2008 Conference and Expo, New Orleans, LA, USA, 16–20 March 2008.
6. Mu, L.J.; Zhao, W.Z. Investigation on Carbon Dioxide Corrosion Behaviors of 13Cr Stainless Steel in Simulated Strum Water. *Corros. Sci.* **2010**, *2*, 82–89. [[CrossRef](#)]
7. Seiersten, M. Material selection for separation, transportation and disposal of CO<sub>2</sub>. In *CORROSION/2001*; Paper no. 01042; NACE International: Houston, TX, USA, 2001.
8. Cui, Z.D.; Wu, S.L.; Zhu, S.L.; Yang, X.J. Study on corrosion properties of pipelines in simulated produced water saturated with supercritical CO<sub>2</sub>. *Appl. Surf. Sci.* **2006**, *252*, 2368–2374. [[CrossRef](#)]
9. Pfennig, A.; Kranzmann, A. Reliability of pipe steels with different amounts of C and Cr during onshore carbon dioxide injection. *Int. J. Greenh. Gas Control* **2011**, *5*, 757–769. [[CrossRef](#)]
10. Zhang, H.; Zhao, Y.L.; Jiang, Z.D. Effects of temperature on the corrosion behavior of 13Cr martensitic stainless steel during exposure to CO<sub>2</sub> and Cl environment. *Mat. Let.* **2005**, *59*, 3370–3374. [[CrossRef](#)]
11. Alhajji, J.; Reda, M. The effect of alloying elements on the electrochemical corrosion of low residual carbon steels in stagnant CO<sub>2</sub>-saturated brine. *Corros. Sci.* **1993**, *34*, 1899–1911. [[CrossRef](#)]
12. Choi, Y.-S.; Nešić, S. Corrosion behavior of carbon steel in supercritical CO<sub>2</sub>-water environments. No. 09256. In Proceedings of the NACE Corrosion 2008 Conference and Expo, New Orleans, LA, USA, 16–20 March 2008.
13. Jiang, X.; Nešić, S.; Huet, F. The Effect of Electrode Size on Electrochemical Noise Measurements and the Role of Chloride on Localized CO<sub>2</sub> Corrosion of Mild Steel. Paper No. 09575. In Proceedings of the NACE Corrosion 2008 Conference and Expo, New Orleans, LA, USA, 16–20 March 2008.
14. Ahmad, Z.; Allam, I.M.; Abdul, B.; Aleem, J. Effect of environmental factors on the atmospheric corrosion of mild steel in aggressive sea coastal environment. *Anti Corros. Methods Mater.* **2000**, *47*, 215–225. [[CrossRef](#)]
15. Pfennig, A.L.; Bäbler, R. Effect of CO<sub>2</sub> on the stability of steels with 1% and 13% Cr in saline water. *Corros. Sci.* **2009**, *51*, 931–940. [[CrossRef](#)]
16. Pfennig, A.; Kranzmann, A. The role of pit corrosion in engineering the carbon storage site at Ketzin, Germany. *AIR Pollut.* **2010**, *136*, 109–119. [[CrossRef](#)]
17. Pfennig, A.; Zastrow, P.; Kranzmann, A. Influence of heat treatment on the corrosion behavior of stainless steels during CO<sub>2</sub>-sequestration into saline aquifer. *Int. J. Greenh. Gas Control* **2013**, *15*, 213–224. [[CrossRef](#)]
18. Nyborg, R. Controlling Internal Corrosion in Oil and Gas Pipelines. Business Briefing: Exploration & Production. *Oil Gas Rev.* **2005**, *2*, 70–74.
19. Carvalho, D.S.; Joia, C.; Mattos, O. Corrosion rate of iron and iron–chromium alloys in CO<sub>2</sub> medium. *Corros. Sci.* **2005**, *47*, 2974–2986. [[CrossRef](#)]
20. Linter, B.R.; Burstein, G.T. Reactions of pipeline steels in carbon dioxide solutions. *Corr. Sci.* **1999**, *41*, 117–139. [[CrossRef](#)]
21. Wu, S.L.; Cui, Z.D.; Zhao, G.X.; Yan, M.L.; Zhu, S.L.; Yang, X.J. EIS study of the surface film on the surface of carbon steel form supercritical carbon dioxide corrosion. *Appl. Surf. Sci.* **2004**, *228*, 17–25. [[CrossRef](#)]
22. Bülbül, Ş.; Sun, Y. Corrosion behavior of high Cr-Ni cast steels in the HCl solution. *J. Alloys Comp.* **2010**, *598*, 143–147. [[CrossRef](#)]
23. Hou, B.; Li, Y.; Li, Y.; Zhang, J. Effect of alloy elements on the anti-corrosion properties of low alloy steel. *Bull. Mater. Sci* **2000**, *23*, 189–192. [[CrossRef](#)]
24. Cvijović, Z.; Radenković, G. Microstructure and pitting corrosion resistance of annealed duplex stainless steel. *Corros. Sci.* **2006**, *48*, 3887–3906. [[CrossRef](#)]
25. Park, J.-Y.; Park, Y.-S. The effects of heat-treatment parameters on corrosion resistance and phase transformations of 14Cr–3Mo martensitic stainless steel. *Mater. Sci. Eng. A* **2007**, *449–451*, 1131–1134. [[CrossRef](#)]
26. Banaś, J.; Lelek-Borkowska, U.; Mazurkiewicz, B.; Solarski, W. Effect of CO<sub>2</sub> and H<sub>2</sub>S on the composition and stability of passive film on iron alloys in geothermal water. *Electrochimica Acta* **2007**, *52*, 5704–5714. [[CrossRef](#)]
27. Bilmes, P.; Llorente, C.; Méndez, C.; Gervasi, C. Microstructure, heat treatment and pitting corrosion of 13CrNiMo plate and weld metals. *Corros. Sci.* **2009**, *51*, 876–881. [[CrossRef](#)]
28. Zhang, L.; Zhang, W.; Jiang, Y.; Deng, B.; Sun, D.; Li, J. Influence of annealing treatment on the corrosion resistance of lean duplex stainless steel 2101. *Electrochimica Acta* **2009**, *54*, 5387–5392. [[CrossRef](#)]

29. Brown, B.; Parakala, S.R.; Nešić, S. CO<sub>2</sub> corrosion in the presence of trace amounts of H<sub>2</sub>S. paper No. 04736. In Proceedings of the NACE International Corrosion Conference Series: Corrosion 2004, New Orleans, LA, USA, 28 March–1 April 2004.
30. Isfahany, A.N.; Saghafian, H.; Borhani, G. The effect of heat treatment on mechanical properties and corrosion behavior of AISI420 martensitic stainless steel. *J. Alloys Compd.* **2011**, *509*, 3931–3936. [[CrossRef](#)]
31. Lucio-Garcia, M.; Gonzalez-Rodriguez, J.; Casales, M.; Martinez, L.; Chacon-Nava, J.; Neri-Flores, M.; Martinez-Villafañe, A. Effect of heat treatment on H<sub>2</sub>S corrosion of a micro-alloyed C–Mn steel. *Corros. Sci.* **2009**, *51*, 2380–2386. [[CrossRef](#)]
32. Madduri, C.; Prakash, R.V. Corrosion Fatigue Crack Growth Studies in Ni-Cr-Mn steels. *Int. J. Mech. Mat. Eng.* **2010**, *1*, 20–25.
33. Seo, M. Initiation and stability of localized corrosion processes on stainless steels. Electrochemical Society. Corrosion Division, Passivity and localized corrosion: An International Symposium in Honour of Professor Norio Sato. *Electrochem. Soc.* **1999**, 99–27, 483–492.
34. Vignal, V.; Delrue, O.; Peultier, J.; Oltra, R. Critical Factors in Localized Corrosion 5: A Symposium in Honour of Hugh Isaacs. In *Local Mechanical-Electrochemical Behavior of Duplex Stainless Steels*; The Electrochemical Society: Pennington, NJ, USA, 2007; pp. 102–104.
35. Pfennig, A.; Wolf, M.; Böllinghaus, T. Corrosion Fatigue of X46Cr13 in CCS Environment. In *Energy Technology 2016*; Springer Science and Business Media LLC.: New York, NY, USA, 2016; pp. 49–56.
36. Pfennig, A.; Wiegand, R.; Wolf, M.; Bork, C.-P. Corrosion and corrosion fatigue of AISI 420C (X46Cr13) at 60 °C in CO<sub>2</sub>-saturated artificial geothermal brine. *Corros. Sci.* **2013**, *68*, 134–143. [[CrossRef](#)]
37. Han, J.; Yang, Y.; Nešić, S.; Brown, N.B. Roles of passivation and galvanic effects in localized CO<sub>2</sub> corrosion of mild steel. Paper No. 08332. In Proceedings of the NACE Corrosion 2008, New Orleans, LA, USA, 16–20 March 2008.
38. Pfennig, A.; Wolthusen, H.; Zastrow, P.; Kranzmann, A. Evaluation of heat treatment performance of potential pipe steels in CCS-environment. In *Energy Technology 2015*; Springer: Cham, Switzerland, 2015; pp. 15–22.
39. Thomas, J.P.; Wei, R.P. Corrosion fatigue crack growth of steels in aqueous solutions I: Experimental results and modeling the effects of frequency and temperature. *Mater. Sci. Eng.* **1992**, *A159*, 205–221. [[CrossRef](#)]
40. Wei, R.P.; Chiou, S. Corrosion fatigue crack growth and electrochemical reactions for an X-70 linepipe steel in carbonate-bicarbonate solution. *Eng. Fract. Mech.* **1992**, *41*, 463–473. [[CrossRef](#)]
41. Cerisola, G.; Busca, G.; de Anna, P.L. Corrosion fatigue behavior of iron in different aqueous environments. *Mater. Chem. Phys.* **1983**, *9*, 387–403. [[CrossRef](#)]
42. Palin-Luc, T.; Pérez-Mora, R.; Bathias, C.; Domínguez, G.; Paris, P.C.; Arana, J.L. Fatigue crack initiation and growth on a steel in the very high cycle regime with sea water corrosion. *Eng. Fract. Mech.* **2010**, *77*, 1953–1962. [[CrossRef](#)]
43. Yeske, R.A.; Roth, L.D. Environmental effects on fatigue of stainless steel at very high frequencies. In *Ultrasonic Fatigue*; The Metallurgical Society of AIME: New York, NY, USA, 1982; pp. 349–364.
44. Macek, W.; Branco, R.; Szala, M.; Marciniak, Z.; Ulewicz, R.; Sczygiol, N.; Kardasz, P. Profile and Areal Surface Parameters for Fatigue Fracture Characterisation. *Materials* **2020**, *13*, 3691. [[CrossRef](#)]
45. Mazzola, L.; Regazzi, D.; Beretta, S.; Bruni, S. Fatigue assessment of old design axles: Service simulation and life extension. *Proc. Inst. Mech. Eng. Part F J. Rail Rapid Transit* **2014**, *230*, 572–584. [[CrossRef](#)]
46. Beretta, S.; Carboni, M.; Conte, A.L.; Regazzi, D.; Trasatti, S.; Rizzi, M. Crack Growth Studies in Railway Axles under Corrosion Fatigue: Full-scale Experiments and Model Validation. *Procedia Eng.* **2011**, *10*, 3650–3655. [[CrossRef](#)]
47. Carboni, M.; Beretta, S.; Conte, A.L. Research on corrosion fatigue of railway axles. *Insight Non-Destructive Test. Cond. Monit.* **2011**, *53*, 361–367. [[CrossRef](#)]
48. Beretta, S.; Carboni, M.; Regazzi, D. Load interaction effects in propagation lifetime and inspections of railway axles. *Int. J. Fatigue* **2016**, *91*, 423–433. [[CrossRef](#)]
49. Hassani-Gangaraj, S.; Carboni, M.; Guagliano, M. Finite element approach toward an advanced understanding of deep rolling induced residual stresses, and an application to railway axles. *Mater. Des.* **2015**, *83*, 689–703. [[CrossRef](#)]
50. Hu, Y.; Wu, S.; Withers, P.J.; Cao, H.; Chen, P.; Zhang, Y.; Shen, Z.; Vojtek, T.; Hutař, P. Corrosion fatigue lifetime assessment of high-speed railway axle EA4T steel with artificial scratch. *Eng. Fract. Mech.* **2021**, *245*, 107588. [[CrossRef](#)]
51. Wu, S.; Xu, Z.; Kang, G.; He, W. Probabilistic fatigue assessment for high-speed railway axles due to foreign object damages. *Int. J. Fatigue* **2018**, *117*, 90–100. [[CrossRef](#)]
52. Pfennig, A.; Wolf, M. Influence of geothermal environment on the corrosion fatigue behavior of standard duplex stainless steel X2CrNiMoN22-5-32. *J. Phys. Conf. Ser.* **2019**, *1425*, 012183.
53. Yevtushenko, O.; Bäßler, R.; Pfennig, A. Corrosion behavior of Cr13steel in CO<sub>2</sub> saturated brine with high chloride concentration. *Mater. Corros.* **2012**, *62*, 517–521. [[CrossRef](#)]
54. Unigovski, Y.B.; Lothongkum, G.; Gutman, E.M.; Alush, D.; Cohen, R. Low-cycle fatigue behavior of 316L-type stainless steel in chloride solutions. *Corr. Sci.* **2009**, *51*, 3014–3120. [[CrossRef](#)]
55. Brück, S.; Schippl, V.; Schwarz, M.; Christ, H.-J.; Fritzen, C.-P.; Weihe, S. Hydrogen Embrittlement Mechanism in Fatigue Behavior of Austenitic and Martensitic Stainless Steels. *Metals* **2018**, *8*, 339. [[CrossRef](#)]
56. Holtam, C.M.; Baxter, D.P.; Ashcroft, I.A.; Thomson, R.C. Effect of crack depth on fatigue crack growth rates for a C–Mn pipeline steel in a sour environment. *Int. J. Fatigue* **2010**, *32*, 288–296. [[CrossRef](#)]
57. Li, M.-Q.; Wei, Z.-W.; Zhang, F.-S.; Tang, J.-Q. The corrosion fatigue of medium strength structural steels. *Corros. Sci.* **1993**, *34*, 1403–1410. [[CrossRef](#)]

58. Thorbjörnsson, I. Corrosion fatigue testing of eight different steels in an Icelandic geothermal environment. *Mater. Des.* **1995**, *16*, 97–102. [[CrossRef](#)]
59. Russick, E.M.; Poulter, G.A.; Adkins, C.L.J.; Sorensen, N.R. Corrosive Effects of Supercritical Carbon Dioxide and Cosolvents on Metals. *J. Supercrit. Fluids* **1996**, *9*, 43–50. [[CrossRef](#)]
60. Fang, B.Y.; Atrens, A.; Wang, J.Q.; Han, E.H.; Zhu, Z.Y.; Ke, W. Review of stress corrosion cracking of pipeline steels in ‘low’ and ‘high’ pH solutions. *J. Mat. Sci.* **2003**, *38*, 127–132. [[CrossRef](#)]
61. Schmitt-Thomas, K.G. *Schwingungsrissskorrosionsanfälligkeit Verschiedener Werkstoffe in: Korrosion Verstehen—Korrosionsschäden vermeiden, Band 2*; Verlag Irene Kuron: Bonn, Germany, 1994.
62. Roeder, E.; Bassler, H.-J.; Huber, M.; Vollmar, J. Vollmar. Schwingungsrissskorrosionsverhalten des austenitischen Stahles X6CrNiMoTi 17 12 2 in 3%iger NaCl-Lösung unter Umlaufbiegebelastung. *Mater. Corros.* **1992**, *43*, 426–431. [[CrossRef](#)]
63. Spähn, R. *Mechanismen der Schwingungsrissskorrosion und Prüfungen in: Korrosion Verstehen Korrosionsschäden Vermeiden, Band 2*; Verlag Irene Kuron: Bonn, Germany, 1994.
64. Lipp, H.-J. Schwingungsrissskorrosionsuntersuchungen an ferritischen rostfreien Stählen. *Mater. Corros.* **1975**, *26*, 825–831. [[CrossRef](#)]
65. Schmitt-Thomas, K.G.; Häpple, T.; Wunderlich, R. Untersuchung des SwRK-Verhaltens des hochreinen martensitischhärtenden Stahles X5CrNiCuNb 17 4 PH im Vergleich zum weichmartensitischen Stahl X4CrNiMo 16 5 1 ESU in chloridhaltigen wässrigen Lösungen. *Mater. Corros.* **1989**, *40*, 427–436. [[CrossRef](#)]
66. Huneau, B.; Mendez, J. Evaluation of environmental effects on fatigue crack growth behavior of a high strength steel in a saline solution with cathodic protection. *Int. J. Fatigue* **2006**, *28*, 124–131. [[CrossRef](#)]
67. Ebara, R. Corrosion fatigue crack initiation behavior of stainless steels. *Procedia Eng.* **2010**, *2*, 1297–1306. [[CrossRef](#)]
68. Alvarez-Armas, I. Duplex Stainless Steels: Brief History and Some Recent Alloys. *Recent Pat. Mech. Eng.* **2008**, *1*, 51–57. [[CrossRef](#)]
69. Prosek, T.; Le Gac, A.; Thierry, D.; Le Manchet, S.; Lojewski, C.; Fanica, A.; Johansson, E.; Canderyd, C.; Dupouiron, F.; Snauwaert, T.; et al. Low-Temperature Stress Corrosion Cracking of Austenitic and Duplex Stainless Steels Under Chloride Deposits. *Corrosion* **2014**, *70*, 1052–1063. [[CrossRef](#)]
70. Schultze, S.; Göllner, J.; Eick, K.; Veit, P.; Heyse, H. Selektive Korrosion von Duplexstahl. Teil 1: Aussagekraft herkömmlicher und neuartiger Methoden zur Untersuchung des Korrosionsverhaltens von Duplexstahl X2CrNiMoN22-5-3 unter besonderer Berücksichtigung der Mikrostruktur. *Mater. Corros.* **2010**, *52/1*, 26–36. [[CrossRef](#)]
71. Arnold, N.; Gümpel, P.; Heitz, T.W. Chloride induced corrosion on stainless steels at indoor swimming pools atmos-pheres Part 2: Influence of hypochlorite. *Mater. Corros.* **1999**, *49*, 140–145. [[CrossRef](#)]
72. Zhang, W.; Fang, K.; Hu, Y.; Wang, S.; Wang, X. Effect of machining-induced surface residual stress on initiation of stress corrosion cracking in 316 austenitic stainless steel. *Corros. Sci.* **2016**, *108*, 173–184. [[CrossRef](#)]
73. Shahryari, A.; Kamal, W.; Omanovic, S. The effect of surface roughness on the efficiency of the cyclic potentiodynamic passivation (CPP) method in the improvement of general and pitting corrosion resistance of 316LVM stainless steel. *Mater. Lett.* **2008**, *62*, 3906–3909. [[CrossRef](#)]
74. Ahmed, A.A.; Mhaede, M.; Basha, M.; Wollmann, M.; Wagner, L. The effect of shot peening parameters and hydroxyapatite coating on surface properties and corrosion behavior of medical grade AISI 316L stainless steel. *Surf. Coat. Technol.* **2015**, *280*, 347–358. [[CrossRef](#)]
75. Lee, S.M.; Lee, W.G.; Kim, Y.H.; Jang, H. Surface roughness and the corrosion resistance of 21Cr ferritic stainless steel. *Corros. Sci.* **2012**, *63*, 404–409. [[CrossRef](#)]
76. Takemoto, M. *Study on the Failure Threshold Stress Criteria for the Prevention and Mechanism of Stress Corrosion Cracking*; Faculty of Science and Engineering, Aoyama Gakuin University: Tokyo, Japan, 1984.
77. Asma, R.N.; Yuli, P.; Mokhtar, C. Study on the Effect of Surface Finish on Corrosion of Carbon Steel in CO<sub>2</sub> Environment. *J. Appl. Sci.* **2011**, *11*, 2053–2057. [[CrossRef](#)]
78. Lv, J.; Guo, W.; Liang, T. The effect of pre-deformation on corrosion resistance of the passive film formed on 2205 duplex stainless steel. *J. Alloys Compd.* **2016**, *686*, 176–183. [[CrossRef](#)]
79. Pfennig, A.; Wolf, M.; Bork, C.-P.; Trenner, S.; Wiegand, R. Comparison between X5CrNiCuNb16-4 and X46Cr13 under Corrosion Fatigue. Paper No. 3776; In *Corrosion*; NACE International: San Antonio, TX, USA, 2014.
80. Vollmar, J.; Roeder, E. Auswirkungen des elektrochemischen Probenpotentials auf das SwRK-Verhalten des Duplexstahls X2CrNiMoN22-5-3 in NaCl-Lösung. *Werkstoffe und Korrosion* **1994**, *45*, 378–386. [[CrossRef](#)]
81. Evgenya, B.; Hughesa, T.; Eskinba, D. Effect of surface roughness on corrosion behavior of low carbon steelin inhibited 4 M hydrochloric acid under laminar and turbulent flow conditions. *Corr. Sci.* **2016**, *103*, 196–205. [[CrossRef](#)]
82. Sanjurjo, P.; Rodríguez, C.; Pariante, I.F.; Belzunce, F.J.; Canteli, A.F. The influence of shot peening on the fatigue behavior of duplex stainless steels. *Procedia Eng.* **2010**, *2*, 1539–1546. [[CrossRef](#)]
83. Abdulstaa, M.; Mhaede, M.; Wollmann, M.; Wagner, L. Investigating the effects of bulk and surface severe plastic deformation on the fatigue, corrosion behavior and corrosion fatigue of AA5083. *Surf. Coat. Technol.* **2014**, *254*, 244–251. [[CrossRef](#)]
84. Wu, X.; Guan, H.; Han, E.H.; Ke, W.; Katada, Y. Influence of surface finish on fatigue cracking behavior of reactor pressure vessel steel in high temperature water. *Mater. Corros.* **2006**, *57*, 868–871. [[CrossRef](#)]
85. Lo, I.-H.; Tsai, W.-T. Effect of selective dissolution on fatigue crack initiation in 2205 duplex stainless steel. *Corros. Sci.* **2007**, *49*, 1847–1861. [[CrossRef](#)]

86. Mathis, R. Initiation and early growth mechanisms of corrosion fatigue cracks in stainless steels. *J. Mater. Sci.* **1987**, *22*, 907–914. [[CrossRef](#)]
87. Garcia, R.L.; Muñoz-Portero, M.; Garcia-Anton, J. Corrosion behaviour of sensitized and unsensitized Alloy 900 (UNS 1.4462) in concentrated aqueous lithium bromide solutions at different temperatures. *Corros. Sci.* **2010**, *52*, 950–959. [[CrossRef](#)]
88. Forster, A.; Schoner, R.; Förster, H.-J.; Norden, B.; Blaschke, A.-W.; Luckert, J.; Beutler, G.; Gaupp, R.; Rhede, D. Reservoir characterization of a CO<sub>2</sub> storage aquifer: The Upper Triassic Stuttgart Formation in the Northeast German Basin. *Mar. Pet. Geol.* **2010**, *27*, 2156–2172. [[CrossRef](#)]
89. Pfennig, A.; Trenner, S.; Wolf, M.; Bork, C. *Vibration Tests for Determination of Mechanical Behavior in CO<sub>2</sub>-Containing Solutions* in European Corrosion Congress EuroCorr 2013; Estoril Congress Center: Estoril, Portugal, 2013.
90. Wolf, M.; Afanasiev, R.; Böllinghaus, T.; Pfennig, A. Investigation of Corrosion Fatigue of Duplex Steel X2CrNiMoN22-5 3 Exposed to a Geothermal Environment under Different Electrochemical Conditions and Load Types. *Energy Procedia* **2017**, *114*, 5337–5345. [[CrossRef](#)]
91. Pfennig, A.; Gröber, A.; Simkin, R.; Kranzmann, A. Influence of Surface Quality on the Corrosion and Corrosion Fatigue Behavior of High Alloyed Steels Exposed to Different Saline Aquifer Water Environments. *Mater. Int. J. Sci.; Tech.* **2019**, *5*, 609–631. [[CrossRef](#)]
92. Pfennig, A.; Simkin, R.; Gröber, A.; Kranzmann, A. The Role of Surface Texture on the Corrosion Behavior of High Al-loyed Steels Exposed to Different Saline Aquifer Water Environments. In Proceedings of the 14th Greenhouse Gas Control Technologies Conference, Melbourne, Australia, 21–26 October 2018; (GHGT-14). SSRN's eLibrary ISSN 1556-5068. Available online: <https://ssrn.com/abstract=3365580> (accessed on 26 March 2021).
93. Pfennig, A.; Kranzmann, A. Failure of standard duplex stainless steel X2CrNiMoN22-5-3 under corrosion fatigue in geothermal environment. *IOP Conf. Ser. Mater. Sci. Eng.* **2020**, *894*, 93–98.
94. López, D.; Pérez, T.; Simison, S. The influence of microstructure and chemical composition of carbon and low alloy steels in CO<sub>2</sub> corrosion. A state-of-the-art appraisal. *Mater. Des.* **2003**, *24*, 561–575. [[CrossRef](#)]
95. Enerhaug, J. A study of localized corrosion in super martensitic stainless steel weldments. Ph.D. Thesis, Norwegian University of Science and Technology (NTNU), Trondheim, Norway, 2002.
96. Mousavi, S.A.; Sufizadeh, A. Metallurgical investigations of pulsed Nd:YAG laser welding of AISI 321 and AISI 630 stainless steels. *Mater. Des.* **2009**, *30*, 3150–3157. [[CrossRef](#)]
97. Wang, J.; Zou, H. Relationship of microstructure transformation and hardening behavior of type 630 stainless steel. *J. Univ. Sci. Tech. Beijing* **2006**, *3*, 213–221. [[CrossRef](#)]
98. Pfennig, A.; Wolthusen, H.; Kranzmann, A. Unusual Corrosion Behavior of 1.4542 Exposed a Laboratory Saline Aquifer Water CCS-environment. *Energy Procedia* **2017**, *114*, 5229–5240. [[CrossRef](#)]
99. Pfennig, A.; Kranzmann, A. Potential of martensitic stainless steel X5CrNiCuNb 16-4 as pipe steel in corrosive CCS environment. *Int. J. Env. Sci. Dev.* **2017**, *8*, 466–473. [[CrossRef](#)]
100. Pfennig, A.; Heynert, K.; Wolf, M.; Böllinghaus, T. First in-situ Electrochemical Measurement During Fatigue Testing of Injection Pipe Steels to Determine the Reliability of a Saline Aquifer Water CCS-site in the Northern German Basin Original. *Energy Procedia* **2014**, *63*, 5773–5786. [[CrossRef](#)]
101. Förster, A.; Norden, B.; Zinck-Jørgensen, K.; Frykman, P.; Kulenkampff, J.; Spangenberg, E.; Erzinger, J.; Zimmer, M.; Kopp, J.; Borm, G.; et al. Baseline characterization of the CO<sub>2</sub>SINK geological storage site at Ketzin, Germany. *Environ. Geosci.* **2006**, *13*, 145–161. [[CrossRef](#)]
102. Bäßler, R.; Sobetzki, J.; Klapper, H.S. Corrosion Resistance of High-Alloyed Materials in Artificial Geothermal Fluids. In Proceedings of the Corrosion 2013, Orlando, FL, USA, 17 March 2013.
103. Pfennig, A.; HTW University of Applied Sciences Berlin; Kranzmann, A. BAM Federal Institute of Materials Research and Testing Borehole Integrity of Austenitized and Annealed Pipe Steels Suitable for Carbon Capture and Storage (CCS). *Int. J. Mater. Mech. Manuf.* **2017**, *5*, 213–218. [[CrossRef](#)]
104. Pfennig, A.; Wolthusen, H.; Wolf, M.; Kranzmann, A. Effect of heat Treatment of Injection Pipe Steels on the Reliability of a Saline Aquifer Water CCS-site in the Northern German Basin. *Energy Procedia* **2014**, *63*, 5762–5772. [[CrossRef](#)]
105. Pfennig, A.; Kranzmann, A. Effect of CO<sub>2</sub> and pressure on the stability of steels with different amounts of chromium in saline water. *Corros. Sci.* **2012**, *65*, 441–452. [[CrossRef](#)]
106. Pfennig, A.; Wolf, M.; Kranzmann, A. Evaluating corrosion and corrosion fatigue behavior via laboratory testing techniques in highly corrosive CCS-environment. In Proceedings of the GHGT15 the Greenhouse Gas Control Technologies Conference, Abu Dhabi, United Arab Emirates, 15–18 March 2021.
107. Kraus, S.W.; Nolze, G. POWDER CELL—A program for the representation and manipulation of crystal structures and calculation of the resulting X-ray powder patterns. *J. Appl. Cryst.* **1996**, *29*, 301–303. [[CrossRef](#)]
108. Pfennig, A.; Wolf, M.; Kranzmann, A. Effects of saline aquifer water on the corrosion behavior of martensitic stainless steels during exposure to CO<sub>2</sub> environment. In Proceedings of the GHGT15 the Greenhouse Gas Control Technologies Conference, Abu Dhabi, United Arab Emirates, 15–18 March 2021.
109. Pfennig, A.; Wolf, M.; Kranzmann, A. The Role of Surface Texture on the Corrosion Fatigue Behavior of High Alloyed Stainless Steel Exposed to Saline Aquifer Water Environment. *Int. J. Mater. Sci. Eng.* **2019**, *7*, 26–33. [[CrossRef](#)]



110. Kranzmann, A.; Huenert, D.; Rooch, H.; Urban, I.; Schulz, W.; Österle, W. *Reactions at the Interface between Steel and Oxide Scale in wet CO<sub>2</sub> Containing Atmospheres*; NACE Corrosion Conference & Expo: Atlanta, GA, USA, 22–26 March 2009.
111. Zhang, Y.; Gao, K.; Schmitt, G. Corrosion inhibition of steels in aqueous media in contact with supercritical carbon dioxide. In *Proceedings of the EUROCORR 2011 Conference—The European Corrosion Congress*, Stockholm, Sweden, Switzerland, 5–8 September 2011.
112. Wei, L.; Pang, X.; Liu, C.; Gao, K. Formation mechanism and protective property of corrosion product scale on X70 steel under supercritical CO<sub>2</sub> environment. *Corr. Sci.* **2015**, *100*, 404–420. [[CrossRef](#)]
113. Pfennig, A.; Kranzmann, A. Corrosion And Fatigue Of Heat Treated Martensitic Stainless Steel 1.4542 Used For Geothermal Applications. *Matter Int. J. Sci. Technol.* **2019**, *5*, 138–158. [[CrossRef](#)]
114. Schiz, J. Einfluss der Austenitisierungsparameter auf die Korrosionsbeständigkeit von Stählen in CCS-Umgebung. Bachelor's Thesis, HTW Berlin, FB2 Mechanical Engineering, Berlin, Germany, 2011.
115. Pfennig, A.; Wolf, M.; Kranzmann, A. In-situ testing of corrosion and corrosion fatigue behavior of stainless steels in geothermal environment. *Int. Proc. Chem. Biol. Env. Eng.* **2018**, *103*, 13–20.
116. Pfennig, A.; Marcus, W.; Gröber, A.; Böllinghaus, T.; Kranzmann, A. Corrosion Fatigue of 1.4542 Exposed to a Laboratory Saline Aquifer Water CCS-environment. *Energy Procedia* **2017**, *114*, 5219–5228. [[CrossRef](#)]
117. Klein, B. *Versuchsplanung DoE. Edition: 4 Label: De Gruyter Oldenbourg*; De Gruyter Oldenbourg Medium: Berlin, Germany, 2014; p. 371.
118. Choi, Y.-S.; Kim, J.-G.; Park, Y.-S.; Park, J.-Y. Austenitizing treatment influence on the electrochemical corrosion behavior of 0.3C-14Cr-3Mo martensitic stainless steel. *Mater. Lett.* **2007**, *61*, 244–247. [[CrossRef](#)]